Structure of *Calcarisporiella thermophila* Hsp104 Disaggregase that Antagonizes Diverse Proteotoxic Misfolding Events

Karolina Michalska,[1,2,3,10] Kaiming Zhang,[4,10] Zachary M. March,[5,6,10] Catherine Hatzos-Skintges,[1,3] Grigore Pintilie,[4] Lance Bigelow,[1] Laura M. Castellano,[5,7] Leann J. Miles,[5,6] Meredith E. Jackrel,[5] Edward Chuang,[5,7] Robert Jedrzejczak,[1,3] James Shorter,[5,6,7,*] Wah Chiu,[4,8,*] and Andrzej Joachimiak[1,2,3,9,11,*]

[1]Midwest Center for Structural Genomics, Argonne National Laboratory, Argonne, IL 60439, USA
[2]Structural Biology Center, Biosciences Division, Argonne National Laboratory, Argonne, IL 60439, USA
[3]Center for Structural Genomics of Infectious Diseases, Consortium for Advanced Science and Engineering, University of Chicago, Chicago, IL 60637, USA
[4]Department of Bioengineering, and Department of Microbiology and Immunology, James H. Clark Center, Stanford University, Stanford, CA 94305, USA
[5]Department of Biochemistry and Biophysics, Perelman School of Medicine, University of Pennsylvania, Philadelphia, PA 19104, USA
[6]Biochemistry and Molecular Biophysics Graduate Group, Perelman School of Medicine, University of Pennsylvania, Philadelphia, PA 19104, USA
[7]Pharmacology Graduate Group, Perelman School of Medicine, University of Pennsylvania, Philadelphia, PA 19104, USA
[8]SLAC National Accelerator Laboratory, Stanford University, Menlo Park, CA 94025, USA
[9]Department of Biochemistry and Molecular Biology, University of Chicago, Chicago, IL 60637, USA
[10]These authors contributed equally
[11]Lead Contact
*Correspondence: jshorter@pennmedicine.upenn.edu (J.S.), wahc@stanford.edu (W.C.), andrzejj@anl.gov (A.J.)
https://doi.org/10.1016/j.str.2018.11.001

SUMMARY

Hsp104 is an AAA+ protein disaggregase with powerful amyloid-remodeling activity. All nonmetazoan eukaryotes express Hsp104 while eubacteria express an Hsp104 ortholog, ClpB. However, most studies have focused on Hsp104 from *Saccharomyces cerevisiae* and ClpB orthologs from two eubacterial species. Thus, the natural spectrum of Hsp104/ClpB molecular architectures and protein-remodeling activities remains largely unexplored. Here, we report two structures of Hsp104 from the thermophilic fungus *Calcarisporiella thermophila* (*Ct*Hsp104), a 2.70Å crystal structure and 4.0Å cryo-electron microscopy structure. Both structures reveal left-handed, helical assemblies with all domains clearly resolved. We thus provide the highest resolution and most complete view of Hsp104 hexamers to date. We also establish that *Ct*Hsp104 antagonizes several toxic protein-misfolding events *in vivo* where *S. cerevisiae* Hsp104 is ineffective, including rescue of TDP-43, polyglutamine, and α-synuclein toxicity. We suggest that natural Hsp104 variation is an invaluable, untapped resource for illuminating therapeutic disaggregases for fatal neurodegenerative diseases.

INTRODUCTION

During severe stress conditions, the capacity of the cell to protect its proteins can become overwhelmed by excessive misfolding and aggregation. However, once normal conditions are restored, the aggregation process is reversed by specialized disaggregases that reactivate proteins trapped in aggregates. These include the hexameric AAA+ protein Hsp104 (Sweeny and Shorter, 2016). In yeast, Hsp104 provides several selective advantages, including: (1) conferring thermotolerance by refolding proteins trapped in heat-induced aggregates (Sweeny and Shorter, 2016); (2) remodeling amyloid fibrils, which empowers yeast to harness protein-based epigenetic elements (prions) for adaptive purposes (Sweeny and Shorter, 2016); (3) promoting degradation of select substrates (Preston et al., 2018; Ruan et al., 2017); (4) regulating material properties of membraneless organelles (Kroschwald et al., 2015); and (5) promoting yeast longevity and fitness by ensuring partitioning of damaged proteins and aggregates to the mother cell during cell division (Sweeny and Shorter, 2016). Protein disaggregases such as Hsp104 are unique among protein-remodeling factors as they can unfold misfolded and aggregated proteins. This disaggregase activity offers an intriguing therapeutic strategy to restore proteostasis in humans where it has gone awry, as with neurodegeneration (Jackrel and Shorter, 2015).

Hsp104 forms hexamers that harbor a central channel through which substrate is translocated (Sweeny and Shorter, 2016). Each protomer is composed of five domains: an N-terminal domain (NTD) that has roles in substrate recognition and translocation, two nucleotide-binding AAA+ domains (NBDs 1 and 2, further divided into large [L] and small [S] subdomains) that bind and hydrolyze ATP and translocate substrate, a coiled-coiled middle domain (MD) insertion in NBD1 that enables interdomain communication and collaboration with the Hsp70 chaperone system, and a short C-terminal tail (CTT) that has been reported to be necessary for hexamer formation (Figure 1A) (Sweeny and Shorter, 2016).
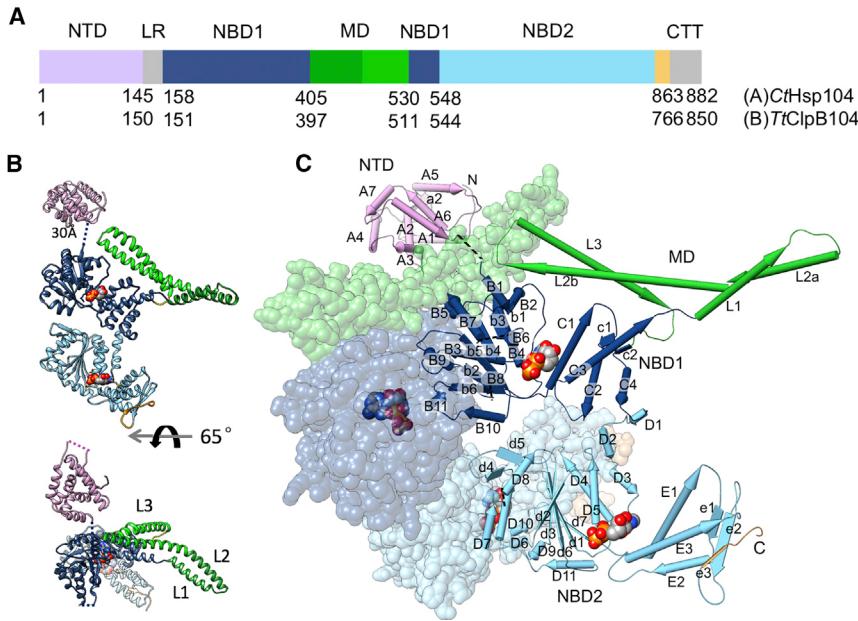
Several structures of bacterial ClpBs and eukaryotic Hsp104s have been reported with varying resolution and complex architecture (Table 1). Low-resolution (11–21 Å) cryo-electron microscopy (cryo-EM) single-particle reconstructions of ClpB from *Thermus thermophilus* (*Tt*ClpB) in the apo state or complexed with ADP (Lee et al., 2007) or AMP-PNP (Lee et al., 2003) show flat hexameric rings with a substantial internal cavity. Similar arrangements were reported for low-resolution cryo-EM structures of an *Escherichia coli* ClpB (*Ec*ClpB) derivative BAP (ClpB variant engineered to interact with ClpP where S722–N748 of ClpB are replaced with V609–I635 of ClpA) complexed with ClpP (Carroni et al., 2014), and for *Saccharomyces cerevisiae* Hsp104 (*Sc*Hsp104) variant Hsp104[N728A] complexed with ADP, ATP, or ATPγS (Wendler et al., 2007, 2009). Only in one case was an attempt made to obtain reconstruction with no symmetry imposed (Wendler et al., 2009); all other models were generated with C6 symmetry. Recently, much higher-resolution (4–5 Å) cryo-EM structures have been reported for *Sc*Hsp104 (Gates et al., 2017; Yokom et al., 2016) and BAP (Deville et al., 2017), which revealed dramatic nucleotide- and substrate-dependent changes in complex architecture. For instance, *Sc*Hsp104 adopts an open left-handed helical hexamer in the presence of AMP-PNP (Gates et al., 2017; Yokom et al., 2016) whereas *Sc*Hsp104 adopts a closed, right-handed helical hexamer when complexed with ATPγS and casein (Gates et al., 2017; Yokom et al., 2016). Additionally, several crystal structures of *Tt*ClpB (Lee et al., 2003), *Ec*ClpB (Carroni et al., 2014) and Hsp104 from *Chaetomium thermophilum* (*Cht*Hsp104) (Heuck et al., 2016) show that protomers are arranged in left-handed helical filaments that are reminiscent of the discrete helical hexamers observed via cryo-EM. The various hexameric models advanced for Hsp104 may represent different stages of the folding pathway or different functional states of the Hsp104 conformational ensemble. However, the quality of the models varies widely. In some structures, only the NBDs and MDs

can be modeled (Carroni et al., 2014; Deville et al., 2017). In two *Ec*ClpB structures, the NTDs have been modeled (PDB: 4D2U, 4D2Q). Thus, to better understand how Hsp104 architecture relates to function, we need a higher-resolution view.

Sequence diversity among Hsp104 orthologs has important functional implications. For instance, *Sc*Hsp104 possesses potent amyloid-remodeling activity necessary for inheritance of beneficial yeast prions, whereas bacterial ClpB has limited ability to remodel amyloid (DeSantis et al., 2012). Moreover, single missense mutations within *Sc*Hsp104 can profoundly enhance functionality (Jackrel et al., 2014; Tariq et al., 2018). At the same time, the vast majority of sequence space among natural Hsp104s remains unexplored. For example, it is unclear whether there are natural Hsp104 orthologs with divergent enhanced or selective activity against misfolded proteins implicated in neurodegenerative diseases, such as α-synuclein (α-Syn) or TDP-43. Indeed, Hsp104 variants with desirable therapeutic disaggregase activity may have arisen through natural selection as an adaptation to unique proteomes and environmental conditions.

Here, we present data that advance our understanding of these two frontiers of Hsp104 structure and function. We determined the structures of Hsp104 from the thermophilic fungus *Calcarisporiella thermophila* (*Ct*Hsp104) in the presence of ADP by X-ray crystallography (at 2.70 Å) and cryo-EM single-particle reconstruction (at 4.0 Å). Moreover, we establish that *Ct*Hsp104 antagonizes several toxic protein-misfolding events where *Sc*Hsp104 is ineffective, including rescue of TDP-43, polyglutamine (polyGlu), and α-Syn toxicity. Thus, we provide evidence for a natural Hsp104 ortholog with enhanced ability to antagonize toxicity linked to neurodegenerative disease.

RESULTS

Crystal Structure of *Ct*Hsp104

We crystallized a double arginine-finger mutant (R328M/R757M) of *Ct*Hsp104 (*Ct*Hsp104[2R]) in complex with ADP. The complex crystallized in the *P*6₅ space group with a single protein chain in the asymmetric unit. We determined its structure by molecular replacement using individual subdomains of ClpB homologs from *T. thermophilus* and *E. coli* as search probes (see STAR

Table 1. Structures of ClpBs and Hsp104s Available in EMD and PDB Sorted by Resolution

Protein[Mutants]	Organism	Ligand	Method	Hexamer Organization	Resolution (Å)	Reference	PDB/EMD ID
BAP[Y503D]	*E. coli*	ATPγS plus ClpP	NS-EM	flat	20	Carroni et al., 2014	4D2X/2559
BAP[E432A]	*E. coli*	ATPγS plus ClpP	NS-EM	flat	18	Carroni et al., 2014	4D2Q/2555
ClpB	*T. thermophilus*	apo	cryo-EM	flat	17.7	Lee et al., 2003	1241
BAP	*E. coli*	ATPγS plus ClpP	NS-EM	flat	17	Carroni et al., 2014	4D2U/2557
ClpB	*T. thermophilus*	ADP	cryo-EM	flat	16.7	Lee et al., 2003	1242
Hsp104[N728A]	*S. cerevisiae*	ATPγS	cryo-EM	flat	13	Wendler et al., 2007	1358/1602
Hsp104[N728A]	*S. cerevisiae*	ADP	cryo-EM	flat	12.8	Wendler et al., 2007	1599
ClpB	*T. thermophilus*	AMP-PNP	cryo-EM	flat	12.1	Lee et al., 2003	1243
Hsp104[N728A]	*S. cerevisiae*	ATP	cryo-EM	flat	11.5	Wendler et al., 2007	1600/1601
ClpB[E271A/E668A]	*T. thermophilus*	ATP	cryo-EM	flat	11.2	Lee et al., 2003	1244
Hsp104[ΔN]	*S. cerevisiae*	ATPγS	cryo-EM	flat	11	Wendler et al., 2007	1359
Hsp104	*S. cerevisiae*	AMP-PNP	cryo-EM	Lh spiral	5.6	Gates et al., 2017; Yokom et al., 2016	5KNE
Hsp104	*S. cerevisiae*	ADP	cryo-EM	Lh spiral	5.6	Gates et al., 2017; Yokom et al., 2016	5VY8/8744
BAP[E279A:E678A]	*E. coli*	ATPγS/casein	cryo-EM	Rh spiral	4.6	Deville et al., 2017	5OFO
BAP[E279A:E678A]	*E. coli*	ATPγS	cryo-EM	Rh spiral	4.5	Deville et al., 2017	5OG1
Hsp104	*S. cerevisiae*	ATPγS/casein extended conformation	cryo-EM	Rh spiral	4.1	Gates et al., 2017; Yokom et al., 2016	5VYA/8746
Hsp104	*S. cerevisiae*	ATPγS/casein closed conformation	cryo-EM	Rh spiral	4.0	Gates et al., 2017; Yokom et al., 2016	5VJH/8697
Hsp104	*C. thermophila*	ADP	cryo-EM	Lh spiral	4.0	this work	6D00/7782
Hsp104	*C. thermophilum*	ADP	X-ray	Lh spiral	3.7	Heuck et al., 2016	5D4W
ClpB[ΔN:E279A:E432A:E678A]	*E. coli*	ADP	X-ray	Lh spiral	3.5	Carroni et al., 2014	4CIU
ClpB	*T. thermophilus*	AMP-PNP	X-ray	Lh spiral	3.0	Lee et al., 2003	1QVR
Hsp104	*C. thermophila*	ADP	X-ray	Lh spiral	2.7	this work	6AZY

Rh and Lh correspond to right- and left-handedness of the oligomer. NS stands for negative staining. BAP refers to a ClpB variant engineered to interact with ClpP where S722-N748 of ClpB are replaced with V609-I635 of ClpA.

Methods). The structure was refined to 2.70Å resolution (Figures 1B and 1C, Table 2).

Similarly to other eukaryotic Hsp104s, *Ct*Hsp104 consists of five domains: NTD (residues 1–144) followed by a 13-residue-long linker 145–157), NBD1 (residues 158–404 and 530–547), MD (residues 405–529), NBD2 (residues 548–862), and CTT (residues 863–882), part of which remains disordered (Figure 1A). In the crystal structure, both NBDs bind ADP (Figures 1B and 1C). The CTT is enriched in acidic residues and is unique to eukaryotic Hsp104s but somewhat variable among orthologs (Figure S1). Conserved channel-facing loops in the NBDs are disordered, including the two canonical tyrosine-containing loops, B6-B7 and D7-D8, which engage translocating substrate and another channel-facing segment, loop B8-B9 (Gates et al., 2017).

Our structure reveals some notable differences compared with previous Hsp104 crystal structures. These include the resolvability and location of the NTD. The NTD is located in close proximity to NBD1 in *Tt*ClpB, whereas the NTD-NBD1 linker in *Ct*Hsp104 is nearly fully extended, positioning the NTD ~30 Å away from NBD1 (Figure 2A). In *Cht*Hsp104 and

*Ec*ClpB structures, NTDs are disordered. Additionally, we observe helix L2 of the MD of *Ct*Hsp104 is bent while helices L3 and L4 are fused into a single long helix L3, similar to the structure of *Cht*Hsp104 (Heuck et al., 2016) (Figures 1B, 1C, 2A, and 2B).

In the crystal lattice, molecules are packed along a 6_5 screw axis to form a left-handed spiral filament with a 16.2-Å rise. This arrangement is similar to the packing previously observed for *Cht*Hsp104 (Heuck et al., 2016), which has ~53% sequence identity with *Ct*Hsp104. In *Cht*Hsp104, the space group was determined as $P2_1$, with three molecules in the asymmetric unit and twinning (Heuck et al., 2016). However, closer inspection suggests that different interpretations, including one in the $P6_5$ space group, are possible. The observed helical motif is reminiscent of the architecture displayed in the crystal structure of *Tt*ClpB (~52% sequence identity with *Ct*Hsp104) (Lee et al., 2003), where the hexagonal symmetry is slightly violated (Figure 2F), and *Ec*ClpB (~49% sequence identity with *Ct*Hsp104) (Carroni et al., 2014). While rather loose packing of the *Tt*ClpB molecules creates a wider central tunnel along the filament, the tighter
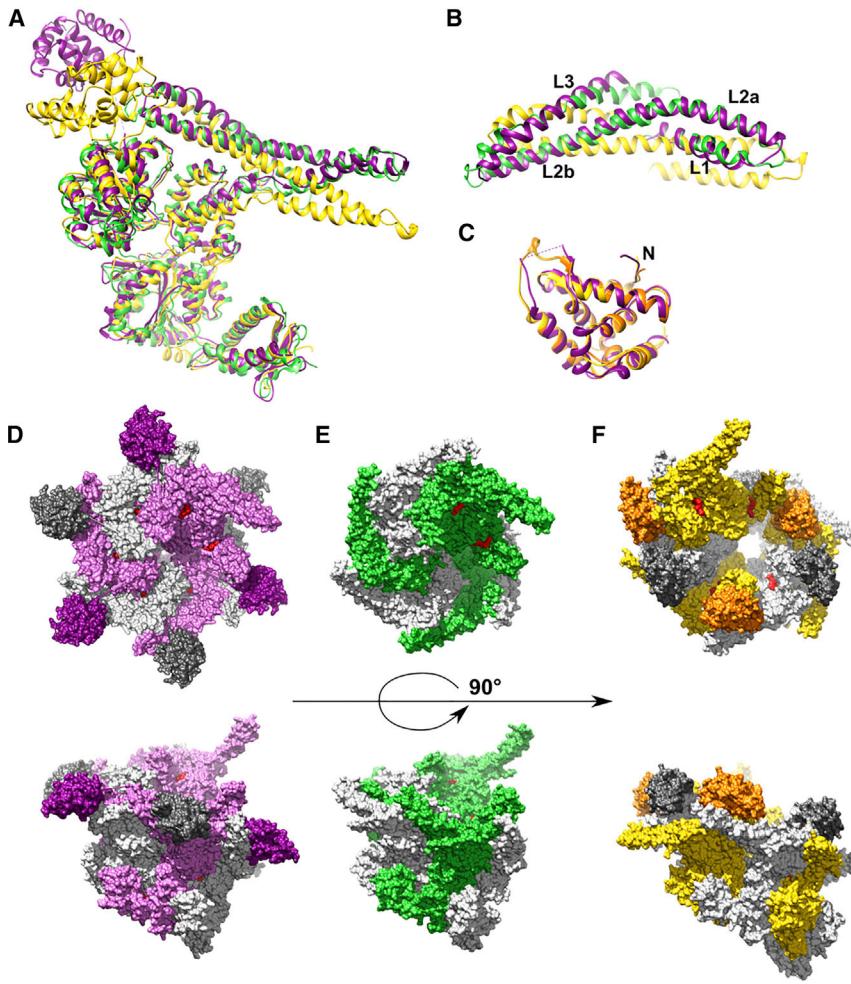
Figure 2. Comparison of Hsp104/ClpB Crystal Structures

(A) Superposition of *Ct*Hsp104 (magenta, this work) with *Cht*Hsp104 (green, chain D [Heuck et al., 2016]) and *Tt*ClpB (yellow, chain B [Lee et al., 2003]).

(B) Superpositions of MDs, with color coding as in (A).

(C) Superpositions of NTDs: *Ct*Hsp104 (magenta), *Tt*ClpB (yellow, chain B) *Tt*ClpB (orange, chain C).

(D–F) Surface representation of *Ct*Hsp104 (D), *Cht*Hsp104 (E), and *Tt*ClpB (F). Every other protomer is colored gray. Darker shades correspond to the N-terminal domain. The ADP nucleotide is shown in red. The minimal "tunnel" seen in *Ct*Hsp104 is a result of incomplete model with residues 248–250 not visible in the electron density maps.

not identical in sequence, obey the general chemical characteristics (hhPxb where h = hydrophobic, x = any, P = proline, and b = basic amino acid).

Cryo-EM Single-Particle Reconstruction of *Ct*Hsp104

Given the apparent nonactive conformation of *Ct*Hsp104 in the crystal, we used cryo-EM single-particle analysis to investigate the structure of wild-type (WT) *Ct*Hsp104 in vitrified solution (Figures 3A and 3B). The reconstructed 3D map (Figure 3C), determined from over 220,000 particles, has a resolution of 4.4 Å unmasked or 4.0 Å masked (Figure 3D). The NBDs and MD are well resolved at 3–5 Å (Figure 3C). However, the flexible NTD-NBD1 linker allows several possible NTD orientations, limiting NTD resolution to ~10 Å (Figure 3C). Further focus classification on the NTD failed to increase resolution (data not shown).

Our cryo-EM structure reveals that *Ct*Hsp104 forms an open one-turn left-handed spiral hexamer, similar to those reported for *Sc*Hsp104 (Yokom et al., 2016) (Figures 3C and 4A–4C). The Cryo-EM map for all domains is visible in each of the six protomers (P1–P6) (Figures 4A–4C, S3, and S4; Video S1). In particular, MDs are resolved well for five protomers (P1–P5), compared with 3/6 for *Sc*Hsp104 maps (Figure S4). All helices in the NBDs matched well with helical densities in the map (Figures 3, 4, 5, and S3–S5).

As in *Sc*Hsp104, NBD1 and NBD2 from the six protomers form a helix, with NBD2 from P1 contacting NBD1 of P6 at the seam (Figure 4A). The MD in P1 reaches across but does not contact the MD of P6 (Figure 4A). Thus, the *Ct*Hsp104 structure observed by cryo-EM is significantly more open than that observed in the crystal. Interestingly, we also found classes (representing ~10% particles) without density for the MD, which shows an even more open cleft (data not shown).

AAA+ interfaces are similar in the crystal filament and cryo-EM hexamer, except for the P1-P6 interface, where we observe

interprotomer associations in *Cht*Hsp104 and *Ct*Hsp104 filaments leave virtually no open tunnel (Figures 2D–2F).

The CTT

The C-terminal region of Hsp104, including a conserved VLPNH motif (V_{857}IRNH$_{861}$ in *Ct*Hsp104) and the acidic stretch of residues unique to eukaryotic orthologs, has been previously named C-terminal domain (CTD). In *Sc*Hsp104, this fragment has been linked to various functions, including cochaperone recruitment (Abbas-Terki et al., 2001) and hexamerization (Mackay et al., 2008). Analysis of the available Hsp104 and ClpB structures indicates that the VLPNH motif rather than being an extension actually belongs to NBD2, whereas the nonglobular fragment, here termed CTT, corresponds to downstream ~20 amino acids (Figures 1A and S2). In *Ct*Hsp104, Val857 (Val889 in *Cht*Hsp104) is part of the e3 β strand while the following section is connected to NBD2 by interactions with helix E3 and the subsequent E3-e2 loop (Figure S2). This association is enabled by nonconserved Arg859, which is typically substituted by a proline residue in other homologs, as seen in *Cht*Hsp104 (Figure S2). In the latter case, no stabilizing hydrogen bonds can be made and the visible portion of the C-terminal region following the e3 strand protrudes from the domain body. A similar arrangement is observed in *Tt*ClpB, in which the e3 strand and its flanking region, though

Table 2. Crystallographic Data Processing and Refinement Statistics

Processing	
Wavelength (Å)	0.9793
Resolution range (Å)[a]	30.00–2.70 (2.75–2.70)
Space group	$P6_5$
Unit cell parameters (Å)	$a = 139.17$, $c = 97.06$
Unique reflections	29,450 (1,467)
Multiplicity	7.3 (7.1)
Completeness (%)	100 (100)
$<I>/<\sigma I>$	23.61 (2.25)
Wilson B factor (Å^2)	49.8
R_{merge}[b]	0.096 (above 1)
$CC_{1/2}$[c]	0.794
CC^{*}[c]	0.941
Refinement	
Resolution (Å)	30.00–2.70
Reflections work/test set	29,413/1,496
R_{work}/R_{free}[d]	0.198/0.249
Average B factor (Å^2) (no. of atoms)	
Macromolecules	74.4 (6,394)
Ligands	82.3 (54)
RMSD bond lengths (Å)	0.008
RMSD bond angles (°)	1.17
Ramachandran favored[e] (%)	97.0
Ramachandran outliers (%)	0
Clashscore[e]	7.91

[a]Values in parentheses correspond to the highest-resolution shell.
[b]$R_{merge} = \Sigma_h \Sigma_j | I_{hj} - <I_h>|/\Sigma_h \Sigma_j I_{hj}$, where I_{hj} is the intensity of observation j of reflection h.
[c]As defined by Karplus and Diederichs (2012).
[d]$R = \Sigma_h |F_o| - |F_c|/\Sigma_h |F_o|$ for all reflections, where F_o and F_c are observed and calculated structure factors, respectively. R_{free} is calculated analogously for the test reflections, randomly selected, and excluded from the refinement.
[e]As defined by MolProbity (Davis et al., 2004).

an atypical interaction between NBD2 from P1 and NBD1 of P6, as reported for ScHsp104 (Gates et al., 2017; Yokom et al., 2016). This interaction generates the spiral architecture. In P1, only NBD2 is supported by the interaction with NBD1 of P6. Nucleotide occupancy in P1 NBD1 is the lowest of the 12 AAA+ domains, although it varies at each binding site across all six protomers (Figure 5C). Interactions between seam protomers also include an interaction between NBD2 (residues 852–854 from the e2-e3 hairpin) of P1 and loop B4-B5 (residues 225–233) of P6. In protomers P2–P6, the C-terminal helix E3 (residues 816–835) from protomer p interacts with helix D4 (residues 575–590) in protomer p-1. Likewise, in protomers P2–P6, the MD of protomer p interacts significantly with the MD and NBD1 of protomer p-1. By contrast, in P1 the MD is largely unbound. Two loops in (p-1)NBD1 are involved in its interaction with the MD, including loop B4-B5 (residues 225–233) (same residues that in P6 contact the P1 NBD2 at the seam) and loop B3-b2.

Nucleotide Binding by CtHsp104

In the crystal structure, protomers interact via canonical AAA+ interfaces: NBD1-NBD1 and NBD2-NBD2 (Figure 1C). In this arrangement, nucleotide-binding sites of both NBDs are occluded by the neighboring protomer, but the ADP ligands are bound exclusively by one NBD chain (Figures 1B and 1C). Specifically, the lower-affinity site in NBD1 (Hattendorf and Lindquist, 2002) shows nucleotide anchored by hydrophobic interactions with the adenine ring and hydrogen bonds between the diphosphoryl group on ADP and the P loop of the NBD (Figures 5A and 5B). The putative arginine fingers from the adjacent protomer, R327, and mutated R328M are located in the same vicinity, but do not participate in nucleotide binding, as seen in the crystal structure (Figure 5B). It is noteworthy that they may only bind to the γ-phosphate of ATP and not necessarily interact with ADP. The side chain of R328M is trapped between helices B9 and B11, whereas the poorly defined R327 appears to stack against helix B11 (Figure 5B). NBD1-NBD1 interactions involve several hydrogen bonds: helix (p-1)B11 interacts with the b3-B6 section (with participation of D239), and loop (p-1)B3-b2 and helix B5 bind to helix C3. R196 from (p-1)B3-b2 also bridges with loop B2-B3 (Figure 5B). The high-affinity site in NBD2 (Hattendorf and Lindquist, 2002) shows the ADP molecule forming a similar pattern of interactions as in NBD1, namely hydrophobic contacts between the base and protein and hydrogen bonds connecting the diphosphoryl group and sugar moiety to the NBD (Figures 5A and 5B). The side chain of the putative (p-1) arginine finger, R757M, is located between helices D12 and D10, more than 8 Å away from the closest oxygen atom of the diphosphoryl moiety (Figure 5B). The protomer-protomer interactions involving NBD2 rely only on two hydrogen bonds between helix (p-1)D4 and helix E1 as well as a single hydrogen bond connecting (p-1)D2 with helix E3. In contrast to NBD1, NBD2L subdomain does not interact with (p-1)NBD2, possibly explaining the high mobility of NBD2 manifesting in poorer electron density and high temperature factors.

The ATP ligand provided with the sample buffer appears to be hydrolyzed as the cryo-EM map is compatible with ADP binding in all NBDs, in a similar arrangement as observed in the crystal structure (Figures 4C and S5; Video S1). Indeed, nucleotide-binding sites in P5 and two nearby arginine residues from P4 are well resolved in the cryo-EM density. R327M, in particular, comes very close to the ADP molecule (Figure S6).

Hexamer Flexibility

Comparison of the crystal and cryo-EM structures highlight dramatic conformational changes in: (1) channel width; (2) helical rise; and (3) NTD, NBD1, and MD orientation (compare Figures 2D–2F, 4C, and 4D). The central channel ranges from the wide pore (25–30 Å) that could accommodate substrate in cryo-EM reconstructions, to a narrow one, as seen in the crystal filaments, which likely represent an inactive state. In all reported structures, the helical rise ranges from 0 to 16 Å within the left-handed spiral hexamers, suggesting a broad spectrum of possible protomer-protomer interfaces, perhaps even a continuum of states between the flat (as reported for some cryo-EM structures) and spiral arrangements (Table 1). This high positional and conformational freedom may enable accommodation of diverse substrates and might promote local refolding of
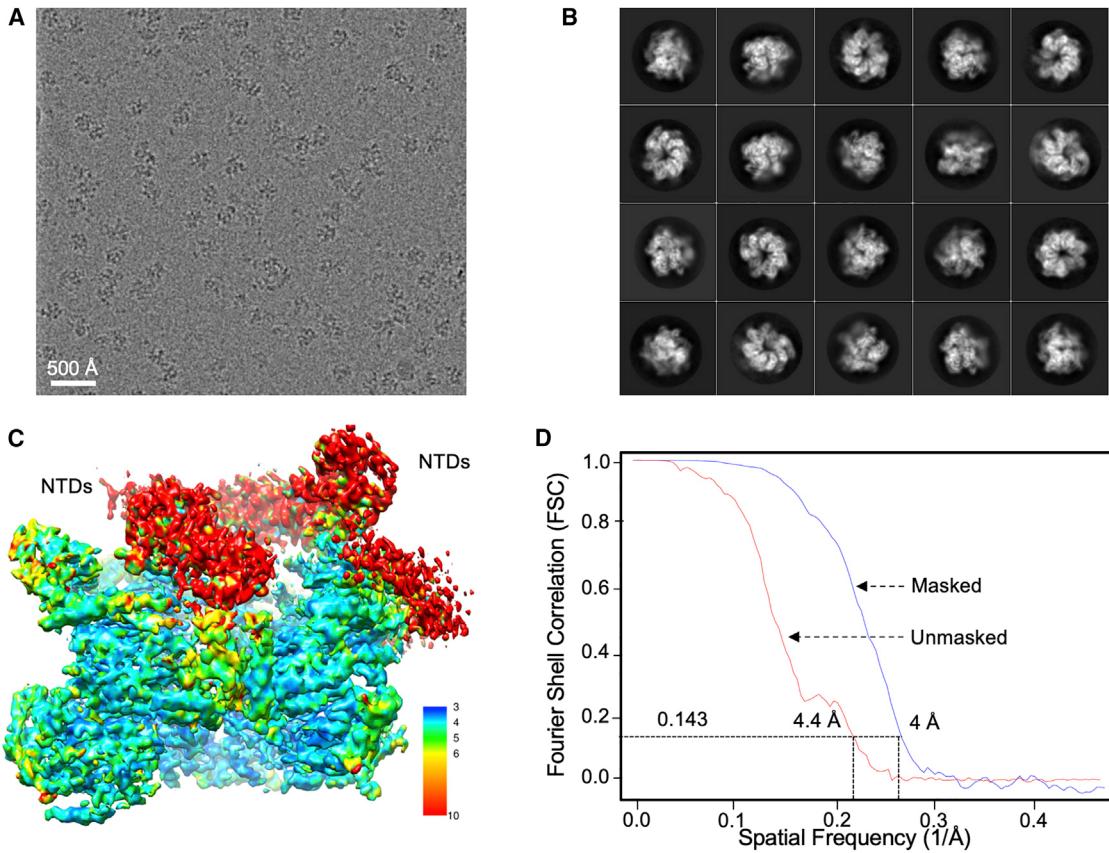
Figure 3. Single Particle 3D Reconstruction of *Ct*Hsp104

(A and B) Cryo-EM micrograph (A) and class averages of *Ct*Hsp104 particles (B).

(C) Resmap coloring of complex, showing higher resolutions for NBDs and lower resolutions for NTDs.

(D) Gold standard Fourier shell correlation plots: 4.4 Å for unmasked map, 4.0 Å for masked map.

substrate secondary structure within the channel. Notably, the orientations of the NTD, NBD1, and MD change drastically between the crystal structure and cryo-EM structure (Figures 4C and 4D). In the crystal structure, the 13-residue linker connecting the NTD with NBD1 is in an extended conformation, placing the NTD ~30 Å outside of the spiral (Figure 4D). Thus, the NTD interacts with the MD on the next protomer without disrupting NBD-NBD contacts (Figures 1B and 4D). In contrast, in the cryo-EM structure the NTD sits on "top" of the hexamer and contacts neighboring NTDs (Figure 4C). The P6 NTD contacts NBD1 on P1, limiting complex size to a hexamer (Figure 4C). Overall, the hexameric assembly extracted from continuous spiral filament in the crystal shares several features with our cryo-EM model and prior reconstructions of *Sc*Hsp104 (Gates et al., 2017; Yokom et al., 2016).

Comparison of *Sc*Hsp104 and *Ct*Hsp104 Structure

Two previous cryo-EM studies on *Sc*Hsp104 have revealed a spiral hexameric architecture, similar to the *Ct*Hsp104 structure (Gates et al., 2017; Yokom et al., 2016). Figure S4 shows each extracted protomer side by side for *Ct*Hsp104, *Sc*Hsp104-AMP-PNP (Yokom et al., 2016), and *Sc*Hsp104-ADP (Gates et al., 2017). The NTDs of *Sc*Hsp104 in the AMP-PNP and ADP

states are visible in P3, P4, and P5, but not for P1, P2, and P6. In *Ct*Hsp104, all protomers have defined NTDs; however, they are not as well resolved as the rest of the map, at only ~10 Å (Figure 3C). MD resolution also varies in each state. Interestingly, in *Sc*Hsp104-AMP-PNP the MD has a slight downward bend, whereas it is more horizontal in our cryo-EM map and model (Figure S4). These slight variations support the hypothesis that MD conformation is affected by the presence and type of nucleotide.

*Ct*Hsp104 Does Not Depend on the NTD or CTT for Hexamerization

To probe the determinants of *Ct*Hsp104 oligomerization in solution, we used size-exclusion chromatography and dynamic light scattering. We tested *Ct*Hsp104 constructs lacking the NTD (*Ct*Hsp104$^{\Delta N}$, residues 153–882) or the NTD and CTT (*Ct*Hsp104$^{\Delta N \Delta C}$, residues 153–864) with or without mutations in the Walker B motifs (E275Q:E679Q) or mutated arginine fingers (R328M/R757M; Table S1). Under low ionic strength conditions (100 mM KCl) all constructs migrate as hexamers in the presence of ATP. Specifically, the *Ct*Hsp104 hexamer is stable at concentrations of 50 μg/mL. Thus, as expected, the NTD is not required for hexamerization of *Ct*Hsp104. However, contrary to *Sc*Hsp104 (Mackay et al., 2008), the CTT is also not required
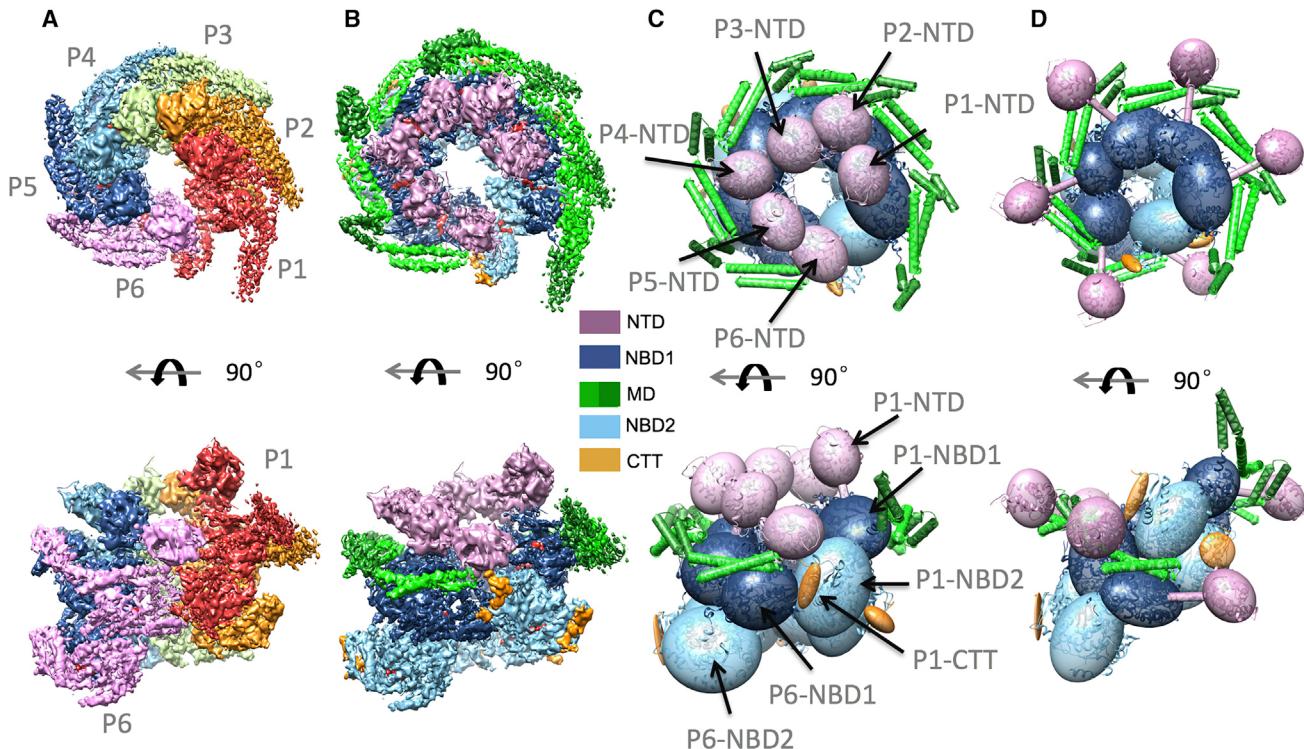
Figure 4. Cryo-EM and X-Ray Structures of *Ct*Hsp104

(A) Segmented complex with each protomer (P1–P6) colored differently in cryo-EM model.

(B) Same structure as in (A), but with each domain colored differently.

(C) Each domain is drawn using a simplified representation (ellipsoid); helices in MD that extend from one protomer to another are drawn as green tubes.

(D) Crystal structure is drawn using a simplified representation (ellipsoid). The NTD domains are in vastly different positions in the crystal compared with the cryo-EM complex, illustrating the high flexibility of the NTD-NBD1 linker.

for *Ct*Hsp104 hexamerization. Indeed, *Ct*Hsp104$^{\Delta N \Delta C}$, which lacks two-thirds of the previously defined longer CTD, formed hexamers. Thus, *Ct*Hsp104 hexamerization is mediated entirely by NBD-NBD interactions.

*Ct*Hsp104 Is an ATP-Driven Disaggregase

Biochemical assays were used to explore *Ct*Hsp104 functionality. First, we measured the ATPase activity of *Ct*Hsp104 and found that it was comparable with *Sc*Hsp104 (Figure 6A). Notably, *Ct*Hsp104 achieved optimal ATPase activity at 65°C, while *Sc*Hsp104 had optimal activity at 42°C (Figure 6B). Thus, *Ct*Hsp104 is likely adapted to function at higher temperatures, in keeping with the thermophilic lifestyle of *C. thermophila*.

We next examined the disaggregase activity of *Ct*Hsp104 *in vitro*. We observed that *Ct*Hsp104 robustly disaggregated and reactivated luciferase aggregates, similar to *Sc*Hsp104 (Figures 6C and 6D). Both *Ct*Hsp104 and *Sc*Hsp104 were inactive alone, but were stimulated by Hsp70 and Hsp40, derived from yeast (Ssa1, Sis1, and Ydj1; Figure 6C) or human (Hsc70, Hdj1, and Hdj2; Figure 6D).

Disaggregation of disordered aggregates by Hsp104 can be induced in the absence of Hsp70 and Hsp40 by the presence of a 1:1 mixture of ATP and ATPγS (Figure 6E) (DeSantis et al., 2012). However, unlike *Sc*Hsp104, *Ct*Hsp104 was completely inactive under these conditions (Figure 6E). We

performed the same disaggregation experiment at 30°C, 37°C, 42°C, and 55°C to determine whether *Ct*Hsp104 may have some Hsp70-independent luciferase disaggregation activity at elevated temperatures where *Ct*Hsp104 has enhanced ATPase activity. However, *Ct*Hsp104 was unable to reactivate aggregated luciferase in every case (Figure S7A). One other possibility is that *Ct*Hsp104 Hsp70-independent disaggregase activity is induced by a different ratio of ATP/ATPγS. For instance, while Hsp70-independent disaggregation by *Sc*Hsp104 is optimally induced by 50% ATPγS, *Sc*Hsp104^{A503V} is optimally induced by 20%–30% ATPγS (Torrente et al., 2016). However, we could not find an ATP/ATPγS mixture that stimulated *Ct*Hsp104 disaggregase activity (Figure S7B). By contrast, *Sc*Hsp104 disaggregase activity was stimulated between 20% and 80% ATPγS (Figure S7B). Thus, *Ct*Hsp104 responds differently than *Sc*Hsp104 and *Ec*ClpB to mixtures of ATP/ATPγS, revealing differences in how *Ct*Hsp104 disaggregase activity is regulated.

*Ct*Hsp104 Rapidly Disassembles SEVI Amyloids

Next, we asked whether *Ct*Hsp104 can disassemble a recalcitrant, ordered amyloid. Thus, we chose SEVI (semen-derived enhancer of virus infection) amyloid fibrils that enhance HIV infection (Castellano et al., 2015). *Sc*Hsp104 remodels SEVI fibrils (Figures 6F and 6G) whereas *Ec*ClpB does not (Castellano
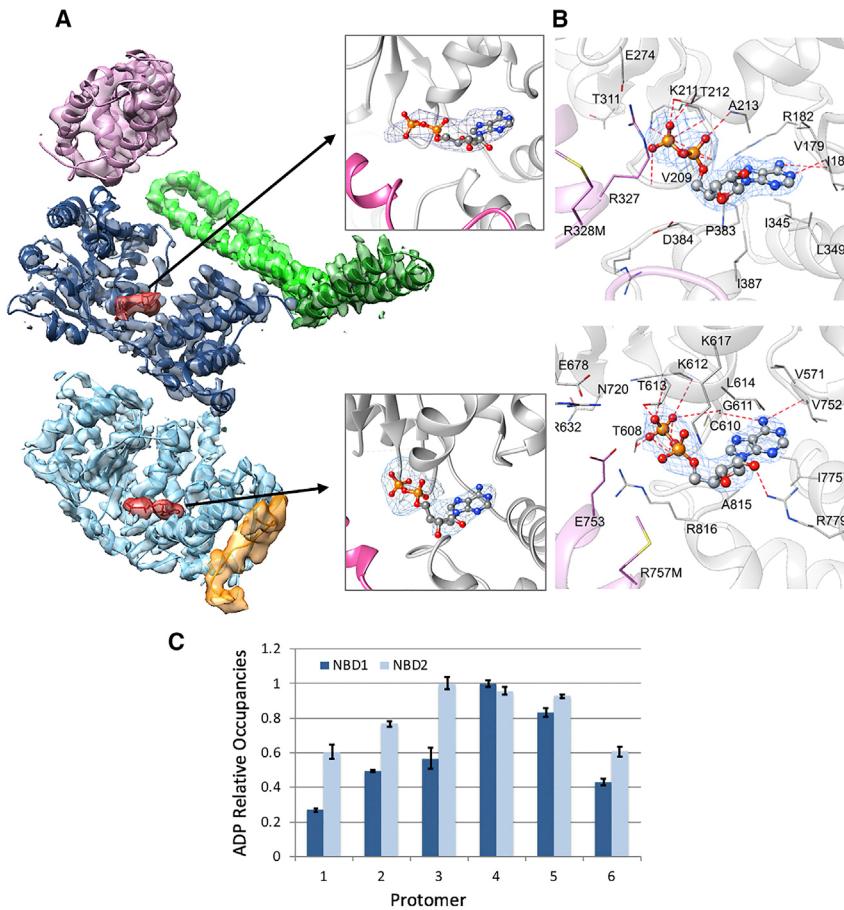
Figure 5. *Ct*Hsp104 Nucleotide-Binding Sites in Cryo-EM Protomer 5 and in the X-Ray Structure

(A) Protomer 5 of the cryo-EM structure, with NBD1 and NBD2 nucleotide-binding pockets enlarged to show detail.

(B) In the crystal structure, the *p* protomer is shown in gray and the (*p*-1) protomer is shown in pink. The ADP moiety is shown in ball-and-stick model in $2mF_o-DF_c$ electron density map contoured at 1σ level.

(C) Relative occupancy of ADP in cryo-EM structure for NBD1 and NBD2 sites in each of protomers 1 through 6.

et al., 2015). *Ct*Hsp104 also rapidly remodeled SEVI fibrils (Figures 6F and 6G). EM revealed that *Ct*Hsp104 and *Sc*Hsp104 remodeled SEVI fibrils into small, amorphous structures (Figures 6F and 6G). Thus, amyloid remodeling is a general property of eukaryotic Hsp104 orthologs, whereas prokaryotic Hsp104 orthologs exhibit reduced amyloid-remodeling activity (Castellano et al., 2015; DeSantis et al., 2012; Shorter and Lindquist, 2004).

*Ct*Hsp104 Complements Thermotolerance Defects of *Δhsp104* Yeast

Next, we defined how *Ct*Hsp104 functions in yeast. *Sc*Hsp104 is essential for acquired thermotolerance in yeast, where it reactivates heat-aggregated proteins (Sweeny and Shorter, 2016). To assess whether *Ct*Hsp104 can complement *Sc*Hsp104 function in thermotolerance, we transformed *Δhsp104* yeast with a plasmid encoding *Ct*Hsp104 under the control of the native *HSP104* promoter. Transformed yeast was pretreated at 37°C for 30 min to induce Hsp104 expression, then exposed to 50°C heat stress for varying times. *Ct*Hsp104 expression conferred thermotolerance to yeast, albeit more weakly than *Sc*Hsp104. After a 20-min heat shock, ∼40% of yeast expressing *Ct*Hsp104 survived compared with ∼75% of yeast expressing *Sc*Hsp104 (Figure 6H). These observations combined with *in vitro* studies (Figure 6C) suggest that *Ct*Hsp104 can collaborate effectively with *Sc*Hsp70 and *Sc*Hsp40, dispelling the

notion of a stringent species barrier between Hsp104 and Hsp70.

CtHsp104 Rescues Diverse Proteotoxicity Models

Next, we asked whether *Ct*Hsp104 could suppress proteotoxicity in yeast associated with expression of several proteins, α-Syn, polyGlu, and TDP-43, involved in human neurodegenerative disease. α-Syn is a lipid-binding protein that normally localizes to the plasma membrane, but mislocalizes to aberrant cytoplasmic inclusions termed Lewy bodies in degenerating dopaminergic neurons in Parkinson's disease (Jackrel and Shorter, 2015). This phenotype can be mimicked in yeast, where overexpression of α-Syn is toxic (Jackrel and Shorter, 2015). Expanded polyGlu tracts in several proteins are sufficient to cause severe neurodegenerative diseases, including Huntington's disease and the spinocerebellar ataxias (Orr and Zoghbi, 2007), and in yeast overexpression of extended polyGlu tracts (e.g., 103Q) is toxic (Duennwald et al., 2006). TDP-43 is an RNA-binding protein with a prion-like domain that mislocalizes from the nucleus and forms cytoplasmic aggregates in degenerating neurons of amyotrophic lateral sclerosis and frontotemporal dementia patients and also forms cytotoxic inclusions in yeast (Jackrel and Shorter, 2015). Coexpression of *Sc*Hsp104 is insufficient to mitigate the aggregation and toxic phenotypes associated with overexpression of any of these proteins (Jackrel et al., 2014) (Figures 7A–7C). However, we have defined a suite of potentiated *Sc*Hsp104 variants such as *Sc*Hsp104[A503S] that can potently suppress toxicity associated with overexpression of TDP-43, α-Syn, and FUS in yeast and metazoa (Jackrel and Shorter, 2015) (Figures 7A–7C). We transformed yeast overexpressing TDP-43, α-Syn, or an expanded polyGlu tract (103Q) with *Ct*Hsp104 to determine whether *Ct*Hsp104 could ameliorate toxicity associated with overexpression of any of these proteins. We observed a modest rescue of TDP-43 toxicity upon *Ct*Hsp104 overexpression, whereas *Sc*Hsp104 was ineffective and *Sc*Hsp104[A503S] strongly suppressed TDP-43 toxicity (Figure 7A). To our surprise, *Ct*Hsp104 robustly rescued α-Syn and polyGlu toxicity (Figures 7B and 7C). Indeed, *Ct*Hsp104 was almost as effective as
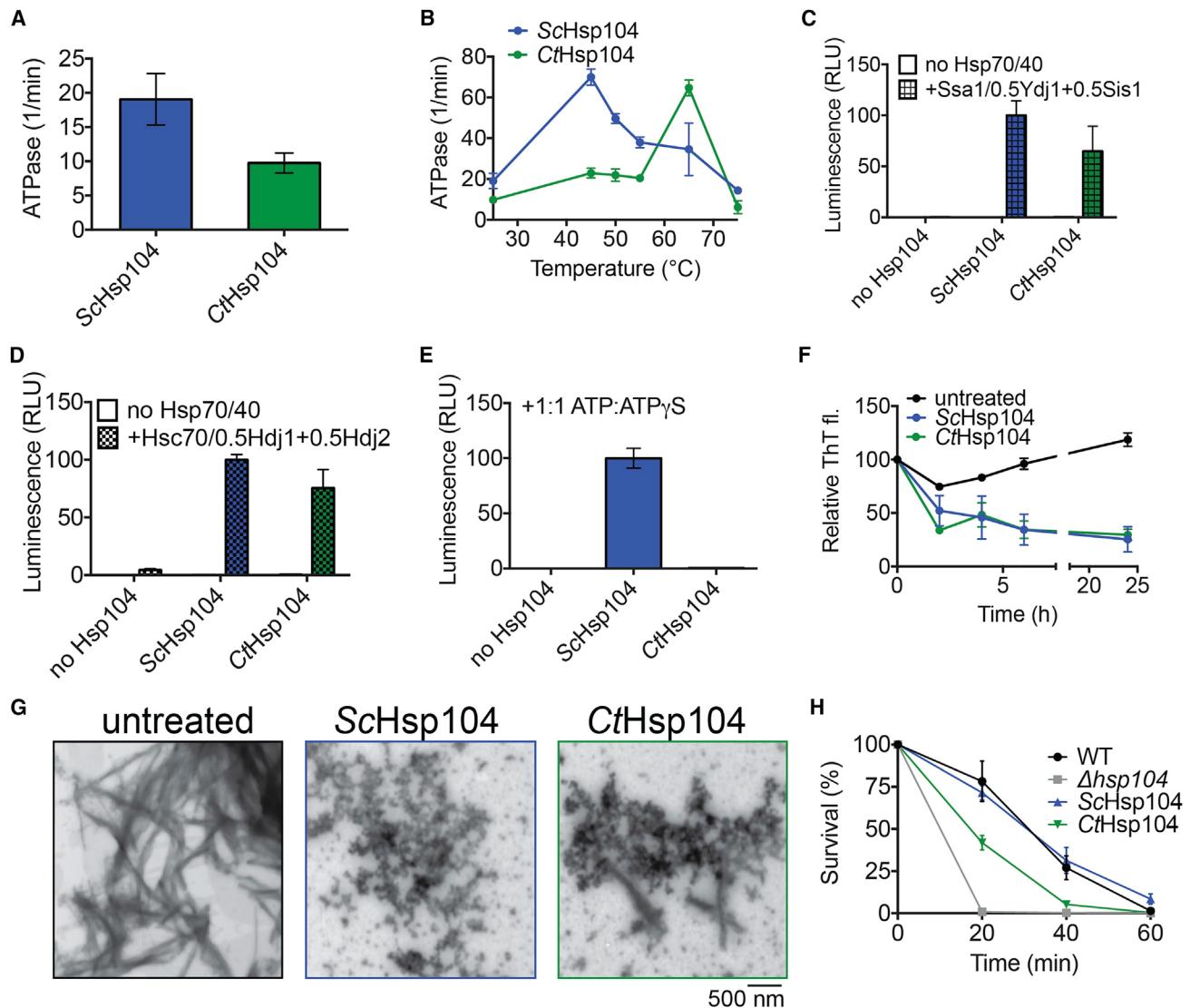
Figure 6. ATPase and Disaggregase Characteristics of *Ct*Hsp104

(A) ATPase activity of *Sc*Hsp104 and *Ct*Hsp104 assessed at 25°C. Values represent means ± SEM (n = 2).

(B) Temperature dependence of *Sc*Hsp104 and *Ct*Hsp104 ATPase activity. Values represent means ± SEM (n = 3).

(C and D) Luciferase aggregates were incubated with *Sc*Hsp104 or *Ct*Hsp104 in the presence or absence of Ssa1 (0.167 µM), and 0.073 µM each Ydj1 and Sis1 (C) or equivalent amounts of Hsc70, Hdj1, and Hdj2 (D). Values represent means ± SEM (n = 4).

(E) Luciferase aggregates were incubated with *Sc*Hsp104 or *Ct*Hsp104 in the presence of a 1:1 mixture of ATP and ATPγS. Values represent means ± SEM (n = 3).

(F) SEVI fibrils (20 µM monomer) were incubated with buffer (untreated), *Sc*Hsp104 (3 µM), or *Ct*Hsp104 (3 µM) for 0–24 hr. Fibril integrity was assessed by ThT fluorescence. Values represent means ± SEM (n = 3–4).

(G) Representative EM images of SEVI fibrils incubated with buffer (untreated), *Sc*Hsp104 (3 µM), or *Ct*Hsp104 (3 µM) for 3 hr. Scale bar is indicated.

(H) *Δhsp104* yeast transformed with plasmids encoding *Sc*Hsp104 or *Ct*Hsp104 under the native *HSP104* promoter heat-shocked at 50°C for the indicated time, cooled on ice, and plated onto SD-His medium. Cells were allowed to recover for 2 days at 30°C and cell viability was assessed. Values represent means ± SEM (n = 3).

*Sc*Hsp104[A503S] in rescuing α-Syn toxicity and similar in efficacy to *Sc*Hsp104[A503S] in rescuing 103Q toxicity (Figures 7B and 7C). By contrast, *Sc*Hsp104 was ineffective (Figures 7B and 7C). Furthermore, rescue of TDP-43, α-Syn, and 103Q toxicity by *Ct*Hsp104 was not due to decreased expression of these disease proteins (Figures 7A–7C). Thus, unlike *Sc*Hsp104, *Ct*Hsp104 is naturally endowed with the ability to combat TDP-43, α-Syn, and 103Q toxicity.

The NTD of Hsp104 has roles in substrate recognition and intersubunit collaboration within hexamers, and deletion of the Hsp104 NTD inhibits potentiated activity against neurodegenerative disease proteins (Sweeny et al., 2015). Hence, we tested whether *Ct*Hsp104[ΔN] suppressed α-Syn and polyGlu toxicity. *Ct*Hsp104[ΔN] suppressed α-Syn and polyGlu toxicity as well as *Ct*Hsp104[WT] (Figure 7D). Thus, the NTD of *Ct*Hsp104 is dispensable for its ability to rescue α-Syn and polyGlu toxicity in yeast.
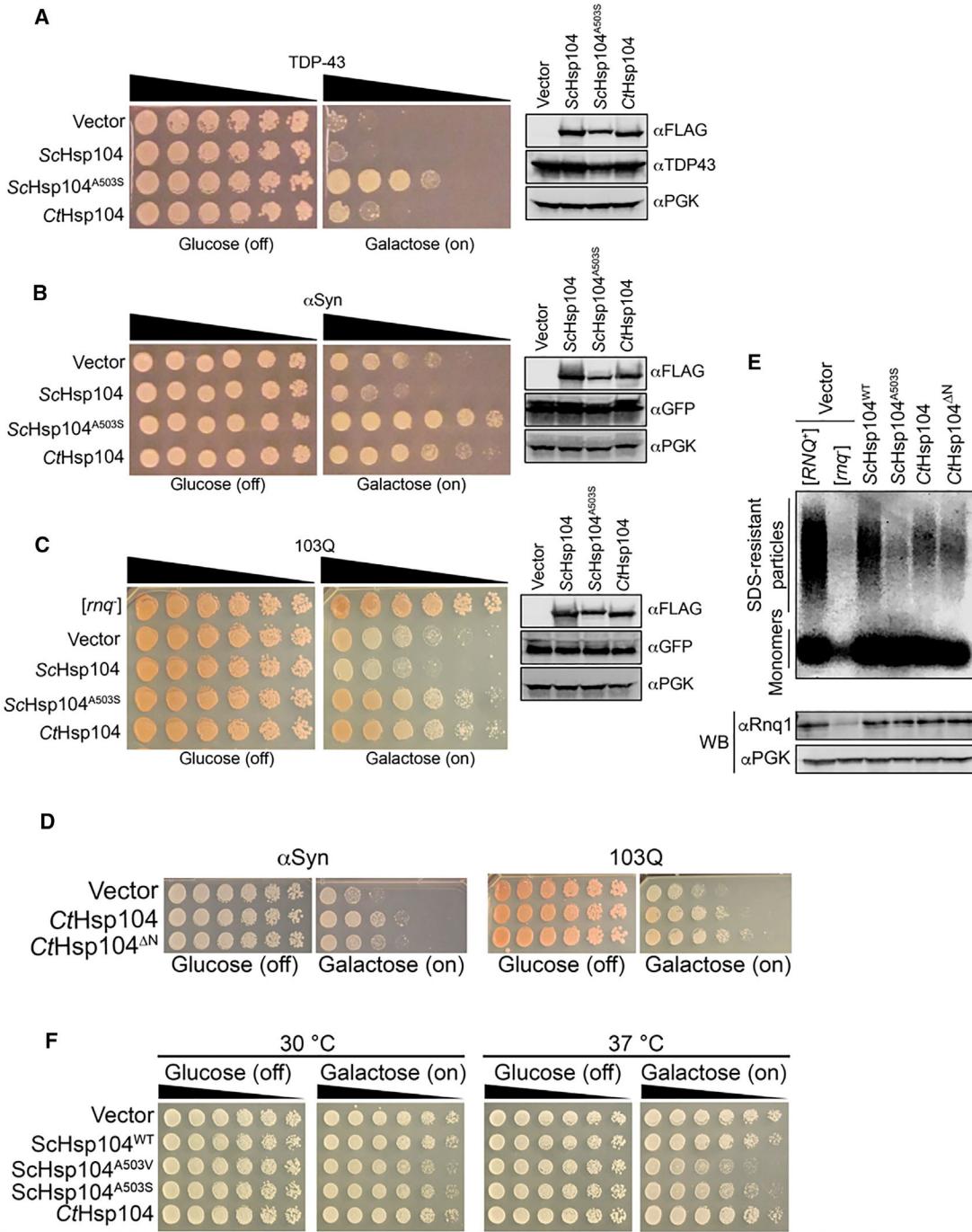
Figure 7. CtHsp104 Rescues Diverse Proteotoxicity Models

(A–C) Δhsp104 yeast transformed with plasmids encoding galactose-inducible TDP-43 (A) or α-Syn-YFP (B) and the indicated galactose-inducible FLAG-tagged Hsp104 were serially diluted 5-fold and spotted onto glucose (expression off) or galactose (expression on). (C) Wild-type yeast transformed with plasmids encoding galactose-inducible 103Q-CFP and the indicated galactose-inducible FLAG-tagged Hsp104 were serially diluted 5-fold and spotted onto glucose (expression off) or galactose (expression on).

(D) Δhsp104 yeast expressing α-Syn-YFP or 103Q-CFP and CtHsp104^WT or CtHsp104^ΔN were serially diluted 5-fold and spotted onto glucose (expression off) or galactose (expression on).

(E) Lysates from yeast expressing 103Q-CFP and the indicated Hsp104 were subjected to SDD-AGE and probed for endogenous Rnq1 prions using a polyclonal anti-Rnq1 antibody. The same lysates were subjected to SDS-PAGE and western blotting for total Rnq1 and PGK to confirm equal loading of samples (bottom).

(F) CtHsp104 does not exhibit reduced growth at 37°C. Hsp104 variants were expressed in the 416GAL vector in Δhsp104 yeast in the absence of any disease protein. The strains were serially diluted 5-fold, spotted in duplicate onto galactose (inducing) and glucose (non-inducing) media, and analyzed at both 30°C and 37°C.

Rescue of polyGlu Toxicity Is Not Simply due to the Elimination of Rnq Prions

Expression of polyGlu proteins is only toxic in yeast that also harbor the prion [RNQ⁺] (Duennwald et al., 2006). Overexpression of polyGlu in [rnq⁻] strains (which lack Rnq1 prions) is nontoxic (Duennwald et al., 2006). Therefore, it is possible that CtHsp104 could rescue polyGlu-associated toxicity either by directly antagonizing polyGlu misfolding and aggregation or through disruption of [RNQ⁺] inheritance. To assess the latter possibility, we monitored the conformational state or Rnq1, the protein determinant of [RNQ⁺], in yeast expressing 103Q and Hsp104 variants using semi-denaturing detergent agarose gel electrophoresis (SDD-AGE). In 103Q yeast transformed with an empty vector, we observed SDS-resistant Rnq1 polymers indicative of Rnq1 prions (Figure 7E). By contrast, an isogenic [rnq⁻] strain was resistant to polyGlu toxicity and lacked SDS-resistant Rnq1 polymers (Figures 7C and 7E). Overexpression of ScHsp104 had little effect on SDS-resistant Rnq1 polymers (Figure 7E). SDS-resistant Rnq1 polymers were reduced in strains expressing ScHsp104^{A503S}, CtHsp104, and CtHsp104^{ΔN} but were still present compared with the [rnq⁻] control, which entirely lacked these species (Figure 7E). Thus, it is unlikely that CtHsp104 or Hsp104^{A503S} rescue of 103Q toxicity is solely due to [RNQ⁺] disruption.

CtHsp104 antagonizes several toxic protein-misfolding events where ScHsp104 is ineffective, including rescue of TDP-43, polyGlu, and α-Syn toxicity. Remarkably, CtHsp104 achieved this rescue without exhibiting any off-target toxicity at 37°C, unlike potentiated Hsp104 variants such as Hsp104^{A503V} or Hsp104^{A503S}, which are toxic to yeast at 37°C (Figure 7F). Thus, CtHsp104 confers enhanced protection against neurodegenerative disease proteins without toxic side effects, a valuable feature for a potential therapeutic agent. These results suggest that natural Hsp104 variation is an invaluable, untapped resource for illuminating therapeutic disaggregases for fatal neurodegenerative diseases.

DISCUSSION

The AAA+ protein disaggregase Hsp104 is conserved in all non-metazoan eukaryotes and eubacteria, although attention has historically been focused on Hsp104 from S. cerevisiae and the bacterial ortholog ClpB. Here, we present the highest-resolution crystal structure combined with cryo-EM single-particle reconstruction of the spiral hexamer in vitrified solution of a eukaryotic Hsp104 ortholog from the thermophilic fungus C. thermophila. The main body of CtHsp104 hexamers is composed of the two AAA+ NBDs that are encircled by the six MDs, forming a ring-like unit in the crystal and interrupted ring in solution. The "top" site, decorated by NTDs that are highly flexible, can adopt very different orientations (Figures 1, 2, and 3), and a "bottom" site renders the location of the CTT. Comparisons of our crystal and cryo-EM structures highlight dramatic conformational changes in (1) channel width, (2) helical rise, and (3) NTD, NBD1, and MD orientations (Figures 2D–2F, 4C, and 4D).

The structures presented here add to a range of structural data demonstrating that Hsp104 forms a highly dynamic assembly. The channel width ranges from the wide pore observed (diameter ∼25–30 Å) in cryo-EM reconstructions that appears to be ready to accept substrate to a very narrow one (diameter ∼8–10 Å), as seen in the crystal filaments, which may represent an inactive state. The helical rise ranges from 0 to 16 Å for all structures, suggesting that Hsp104 may exist in many stable or transient states that evolved to accommodate many protein sequences (DeSantis et al., 2012). Notably, the relative orientations of the NTD, NBD1, and MD change dramatically between our crystal structure and cryo-EM structure. In the crystal the NTD is located away from the hexamer, allowing the MD to intercalate between NBD1 and the NTD. By contrast, in the cryo-EM structure the NTDs are located over the central channel of the hexamer and MDs wrap around adjacent NBD1s, consistent with previous reports (Yokom et al., 2016). We suggest that these conformational rearrangements are involved in the formation and function of Hsp104 hexamers and suggest a possible "breathing motion" in the hexamer, complementing the large conformational changes upon ATP hydrolysis documented by others (Gates et al., 2017; Sweeny et al., 2015; Sweeny and Shorter, 2016; Yokom et al., 2016). Overall our findings support the conformational flexibility of Hsp104, and we suggest that such flexibility may be a generic feature of AAA+ proteins, facilitating torque generation to translocate substrate (van den Boom and Meyer, 2018; Zehr et al., 2017).

The cryo-EM structure shows that ADP occupancy differs across all six protomers (Figure 5C). ATP binding and hydrolysis drive conformational changes, which presumably enable translocation of the protein through the central channel of the hexameric assembly. The cryo-EM structure provides some indication about conformational differences between ADP-bound and ADP-free states, as illustrated in Figure S8. Two helices (C1 and C3) of NBD1, which are adjacent to the nucleotide-binding site, are directly connected to the MD. In our map several bulky side chains in this area are moderately resolved, e.g., D384 close to the ADP binding site, Y353, D391, H356, and H357 in the middle of the two helices, and R399, R469, and Y458 close to where they contact the MD. While at ∼4-Å resolution we cannot be fully certain of side-chain placements and potential salt bridges, the α helices themselves are well resolved in all protomers, hence we are certain of their position (within ∼1 Å positional error). Moreover, the crystal structure solved at 2.70-Å resolution provides more details of this network of interactions that connects MD, C1, C3, and the nucleotide-binding site. Severing these interactions will likely affect ATP binding and hydrolysis (Jackrel et al., 2015; Lipinska et al., 2013).

To compare the conformations of the C1 and C3 helices for ADP-bound and ADP-less states, we aligned the protomers P1 (lowest ADP occupancy) and P4 (highest ADP occupancy) by aligning all residues in the NBD1 except for the C1 and C3 helices. The superposition is shown in Figure S8B. The two helices in protomer P1, the ADP-less-like state, are highlighted in bright red and can be seen to be extending outward from the ADP site, whereas the helices in protomer P4, the ADP-bound state, highlighted in bright blue, can be seen to be drawn in toward the ADP molecule (possibly because of the D384 residue). The difference in positions can be expressed roughly as a shift of ∼10 Å and rotation of ∼20°. The connection of these helices to the MD in turn appears to result in the MD of P1 being in a more "open" position (more outward from the center of the complex) compared with the MD domain in protomer P4.

The "bottom" of the hexamer is much more open and feature-less, with CTTs extending from NBD2 toward the outer edges of the assembly, about 25 Å from the central channel exit. Our structures indicate that CTT is not a structural domain and show that the portion of previously identified CTD belongs to NBD2 (Figure S2). Notably, CTT remains disordered in both crystal and cryo-EM structures, indicating that this element does not participate in assembly stabilization. Indeed, deletion of 24 C-terminal residues does not impair hexamerization (Table S1). Two acidic motifs (DEDM and EDED) in the CTT are somewhat conserved among Hsp104s (Figure S2), and for ScHsp104 have been implicated in cochaperone binding and ATPase activity (Abbas-Terki et al., 2001; Mackay et al., 2008). Possibly in CtHsp104 it also modulates interactions with helper proteins such as Sti1, in analogy to similar motifs found in Hsp70 and Hsp90 (Abbas-Terki et al., 2001; Yu et al., 2015). Indeed, C-terminal acidic residues of Hsp104 are critical in curing some Sup35 prion variants, as are cochaperones such as Sti1, which interact with this region of Hsp104 (Gorkovskiy et al., 2017; Zhao et al., 2017). Thus, these acidic motifs may indirectly facilitate processing and folding of substrates by recruiting downstream cochaperones.

We have additionally established a range of activities for CtHsp104 in vitro and in vivo. CtHsp104 functionally complements ScHsp104 in acquired thermotolerance in yeast, and remodels SEVI amyloid fibrils in vitro. Intriguingly, CtHsp104 is able to robustly suppress toxicity of diverse proteins associated with neurodegenerative diseases, including α-Syn, polyGlu, and TDP-43, similar to previously defined potentiated Hsp104 variants (Jackrel et al., 2014, 2015). However, the biochemical activity of CtHsp104 more closely resembles wild-type ScHsp104 rather than potentiated Hsp104s (e.g., no elevated ATPase or disaggregase activity) (Jackrel et al., 2014; Tariq et al., 2018; Torrente et al., 2016). Thus, the ability of CtHsp104 to potently rescue TDP-43, polyGlu, and α-Syn toxicity may result from differences in substrate recognition between CtHsp104 and ScHsp104. These potential differences in substrate recognition were not due to the NTD of CtHsp104, as CtHsp104$^{\Delta N}$ could rescue polyGlu and α-Syn toxicity in yeast as effectively as CtHsp104. An interesting direction for future studies will be to determine the factors underlying substrate recognition by CtHsp104.

Our results establish that a natural Hsp104 ortholog can robustly antagonize proteotoxic misfolding where ScHsp104 is inactive, which has important implications in engineering disaggregases for therapeutic modalities. Sequence variation among homologous proteins is recognized as a valuable reservoir for rapid exploration of a protein sequence space in directed evolution studies (Crameri et al., 1998). Recent studies have demonstrated that molecular evolution techniques such as ancestral protein reconstruction can improve the pharmacologic properties of a protein-based drug (Zakas et al., 2017). Therefore, it will be important to determine whether other Hsp104 homologs are capable of suppressing proteotoxicity where ScHsp104 cannot, which may further illuminate the design of therapeutic disaggregases.

The loss of Hsp104 from metazoan lineages was abrupt (Erives and Fassler, 2015). The reason for this loss is unknown. It is also not known why Hsp104 is not naturally potentiated.

One possible explanation is that Hsp104 may have been lost by a negative selection event, since potentiated Hsp104s can have deleterious side effects, e.g., promiscuous unfoldase activity that causes increased temperature sensitivity, and disrupted prion inheritance (Jackrel and Shorter, 2015). However, here we have established that the Hsp104 ortholog CtHsp104 is naturally endowed with a range of therapeutic protein-remodeling activities while being well tolerated by host organisms such as yeast and seemingly devoid of discernible deleterious effects. Thus, it will be very interesting to understand the basis of this possible alternative mode of enhanced activity and to discover whether similar activity is seen in other Hsp104 orthologs.

STAR★METHODS

Detailed methods are provided in the online version of this paper and include the following:

- KEY RESOURCES TABLE
- CONTACT FOR REAGENT AND RESOURCE SHARING
- EXPERIMENTAL MODEL AND SUBJECT DETAIL
  - Yeast Strains and Media
- METHOD DETAILS
  - Plasmids
  - CtHsp104^{2R} Preparation for Crystallization
  - Preparation of CtHsp104 and Deletion Mutants for Cryo-EM, SEC and DLS
  - Size Exclusion Chromatography of CtHsp104 and Deletion Mutants
  - Protein Crystallization
  - X-ray Data Collection, Structure Determination and Refinement
  - Cryo-Electron Microscopy Data Acquisition
  - Single Particle Image Processing and 3D Reconstruction
  - Segmentation and Fitting
  - Proteins for Biochemical Assays
  - ATPase Assay
  - Luciferase Reactivation Assay
  - Semen-Derived Enhancer of Virus Infection (SEVI) Remodeling
  - Yeast Strains and Media
  - Yeast Transformation and Spotting Assays
  - Thermotolerance
  - Semi-Denaturing Detergent Agarose Gel Electrophoresis (SDD-AGE)
- QUANTIFICATION AND STATISTICAL ANALYSIS

REFERENCES

Abbas-Terki, T., Donze, O., Briand, P.A., and Picard, D. (2001). Hsp104 interacts with Hsp90 cochaperones in respiring yeast. Mol. Cell. Biol. 21, 7569–7575.

Adams, P.D., Baker, D., Brunger, A.T., Das, R., DiMaio, F., Read, R.J., Richardson, D.C., Richardson, J.S., and Terwilliger, T.C. (2013). Advances, interactions, and future developments in the CNS, Phenix, and Rosetta structural biology software systems. Annu. Rev. Biophys. 42, 265–287.

Afonine, P.V., Grosse-Kunstleve, R.W., Echols, N., Headd, J.J., Moriarty, N.W., Mustyakimov, M., Terwilliger, T.C., Urzhumtsev, A., Zwart, P.H., and Adams, P.D. (2012). Towards automated crystallographic structure refinement with phenix.refine. Acta Crystallogr. D Biol. Crystallogr. 68, 352–367.

Carroni, M., Kummer, E., Oguchi, Y., Wendler, P., Clare, D.K., Sinning, I., Kopp, J., Mogk, A., Bukau, B., and Saibil, H.R. (2014). Head-to-tail interactions of the coiled-coil domains regulate ClpB activity and cooperation with Hsp70 in protein disaggregation. Elife 3, e02481.

Castellano, L.M., Bart, S.M., Holmes, V.M., Weissman, D., and Shorter, J. (2015). Repurposing Hsp104 to antagonize seminal amyloid and counter HIV. Infect. Chem. Biol. 22, 1074–1086.

Cowtan, K. (2006). The Buccaneer software for automated model building. 1. Tracing protein chains. Acta Crystallogr. D Biol. Crystallogr. 62, 1002–1011.

Crameri, A., Raillard, S.A., Bermudez, E., and Stemmer, W.P. (1998). DNA shuffling of a family of genes from diverse species accelerates directed evolution. Nature 391, 288–291.

Davis, I.W., Murray, L.W., Richardson, J.S., and Richardson, D.C. (2004). MOLPROBITY: structure validation and all-atom contact analysis for nucleic acids and their complexes. Nucleic Acids Res. 32, W615–W619.

DeSantis, M.E., Leung, E.H., Sweeny, E.A., Jackrel, M.E., Cushman-Nick, M., Neuhaus-Follini, A., Vashist, S., Sochor, M.A., Knight, M.N., and Shorter, J. (2012). Operational plasticity enables hsp104 to disaggregate diverse amyloid and nonamyloid clients. Cell 151, 778–793.

DeSantis, M.E., Sweeny, E.A., Snead, D., Leung, E.H., Go, M.S., Gupta, K., Wendler, P., and Shorter, J. (2014). Conserved distal loop residues in the Hsp104 and ClpB middle domain contact nucleotide-binding domain 2 and enable Hsp70-dependent protein disaggregation. J. Biol. Chem. 289, 848–867.

Deville, C., Carroni, M., Franke, K.B., Topf, M., Bukau, B., Mogk, A., and Saibil, H.R. (2017). Structural pathway of regulated substrate transfer and threading through an Hsp100 disaggregase. Sci. Adv. 3, e1701726.

Duennwald, M.L., Jagadish, S., Giorgini, F., Muchowski, P.J., and Lindquist, S. (2006). A network of protein interactions determines polyglutamine toxicity. Proc. Natl. Acad. Sci. U S A 103, 11051–11056.

Duennwald, M.L., and Lindquist, S. (2008). Impaired ERAD and ER stress are early and specific events in polyglutamine toxicity. Genes Dev. 22, 3308–3319.

Emsley, P., and Cowtan, K. (2004). Coot: model-building tools for molecular graphics. Acta Crystallogr. D Biol. Crystallogr. 60, 2126–2132.

Erives, A.J., and Fassler, J.S. (2015). Metabolic and chaperone gene loss marks the origin of animals: evidence for Hsp104 and Hsp78 chaperones sharing mitochondrial enzymes as clients. PLoS One 10, e0117192.

French, S., and Wilson, K. (1978). Treatment of negative intensity observations. Acta Crystallogr. A 34, 517–525.

Gates, S.N., Yokom, A.L., Lin, J., Jackrel, M.E., Rizo, A.N., Kendsersky, N.M., Buell, C.E., Sweeny, E.A., Mack, K.L., Chuang, E., et al. (2017). Ratchet-like polypeptide translocation mechanism of the AAA+ disaggregase Hsp104. Science 357, 273–279.

Gietz, R.D., and Schiestl, R.H. (2007). High-efficiency yeast transformation using the LiAc/SS Carrier DNA/PEG method. Nat. Protoc. 2, 31–34.

Gitler, A.D., Bevis, B.J., Shorter, J., Strathearn, K.E., Hamamichi, S., Su, L.J., Caldwell, K.A., Caldwell, G.A., Rochet, J.C., McCaffery, J.M., et al. (2008). The Parkinson's disease protein alpha-synuclein disrupts cellular Rab homeostasis. Proc. Natl. Acad. Sci. U S A 105, 145–150.

Gorkovskiy, A., Reidy, M., Masison, D.C., and Wickner, R.B. (2017). Hsp104 disaggregase at normal levels cures many [PSI(+)] prion variants in a process promoted by Sti1p, Hsp90, and Sis1p. Proc. Natl. Acad. Sci. U S A 114, E4193–E4202.

Halfmann, R., and Lindquist, S. (2008). Screening for amyloid aggregation by semi-denaturing detergent-agarose gel electrophoresis. J. Vis. Exp. 17, 838.

Hattendorf, D.A., and Lindquist, S.L. (2002). Cooperative kinetics of both Hsp104 ATPase domains and interdomain communication revealed by AAA sensor-1 mutants. EMBO J. 21, 12–21.

Heuck, A., Schitter-Sollner, S., Suskiewicz, M.J., Kurzbauer, R., Kley, J., Schleiffer, A., Rombaut, P., Herzog, F., and Clausen, T. (2016). Structural basis for the disaggregase activity and regulation of Hsp104. Elife 5, https://doi.org/10.7554/eLife.21516.

Jackrel, M.E., DeSantis, M.E., Martinez, B.A., Castellano, L.M., Stewart, R.M., Caldwell, K.A., Caldwell, G.A., and Shorter, J. (2014). Potentiated Hsp104 variants antagonize diverse proteotoxic misfolding events. Cell 156, 170–182.

Jackrel, M.E., and Shorter, J. (2015). Engineering enhanced protein disaggregases for neurodegenerative disease. Prion 9, 90–109.

Jackrel, M.E., Yee, K., Tariq, A., Chen, A.I., and Shorter, J. (2015). Disparate mutations confer therapeutic gain of Hsp104 function. ACS Chem. Biol. 10, 2672–2679.

Johnson, B.S., Snead, D., Lee, J.J., McCaffery, J.M., Shorter, J., and Gitler, A.D. (2009). TDP-43 is intrinsically aggregation-prone, and amyotrophic lateral sclerosis-linked mutations accelerate aggregation and increase toxicity. J Biol. Chem. 284, 20329–20339.

Karplus, P.A., and Diederichs, K. (2012). Linking crystallographic model and data quality. Science 336, 1030–1033.

Kim, Y., Babnigg, G., Jedrzejczak, R., Eschenfeldt, W.H., Li, H., Maltseva, N., Hatzos-Skintges, C., Gu, M., Makowska-Grzyska, M., Wu, R., et al. (2011). High-throughput protein purification and quality assessment for crystallization. Methods 55, 12–28.

Klock, H.E., and Lesley, S.A. (2009). The polymerase incomplete primer extension (PIPE) method applied to high-throughput cloning and site-directed mutagenesis. Methods Mol. Biol. 498, 91–103.

Kroschwald, S., Maharana, S., Mateju, D., Malinovska, L., Nuske, E., Poser, I., Richter, D., and Alberti, S. (2015). Promiscuous interactions and protein disaggregases determine the material state of stress-inducible RNP granules. Elife 4, e06807.

Lee, S., Choi, J.M., and Tsai, F.T. (2007). Visualizing the ATPase cycle in a protein disaggregating machine: structural basis for substrate binding by ClpB. Mol. Cell 25, 261–271.

Lee, S., Sowa, M.E., Watanabe, Y.H., Sigler, P.B., Chiu, W., Yoshida, M., and Tsai, F.T. (2003). The structure of ClpB: a molecular chaperone that rescues proteins from an aggregated state. Cell 115, 229–240.

Lipinska, N., Zietkiewicz, S., Sobczak, A., Jurczyk, A., Potocki, W., Morawiec, E., Wawrzycka, A., Gumowski, K., Slusarz, M., Rodziewicz-Motowidlo, S., et al. (2013). Disruption of ionic interactions between the nucleotide binding domain 1 (NBD1) and middle (M) domain in Hsp100 disaggregase unleashes toxic hyperactivity and partial independence from Hsp70. J. Biol. Chem. 288, 2857–2869.

Mackay, R.G., Helsen, C.W., Tkach, J.M., and Glover, J.R. (2008). The C-terminal extension of Saccharomyces cerevisiae Hsp104 plays a role in oligomer assembly. Biochemistry 47, 1918–1927.

McCoy, A.J., Grosse-Kunstleve, R.W., Adams, P.D., Winn, M.D., Storoni, L.C., and Read, R.J. (2007). Phaser crystallographic software. J. Appl. Crystallogr. 40, 658–674.

Minor, W., Cymborowski, M., Otwinowski, Z., and Chruszcz, M. (2006). HKL-3000: the integration of data reduction and structure solution–from diffraction images to an initial model in minutes. Acta Crystallogr. D Biol. Crystallogr. 62, 859–866.

Neumann, M., Sampathu, D.M., Kwong, L.K., Truax, A.C., Micsenyi, M.C., Chou, T.T., Bruce, J., Schuck, T., Grossman, M., Clark, C.M., et al. (2006). Ubiquitinated TDP-43 in frontotemporal lobar degeneration and amyotrophic lateral sclerosis. Science 314, 130–133.

Orr, H.T., and Zoghbi, H.Y. (2007). Trinucleotide repeat disorders. Annu. Rev. Neurosci. 30, 575–621.

Padilla, J.E., and Yeates, T.O. (2003). A statistic for local intensity differences: robustness to anisotropy and pseudo-centering and utility for detecting twinning. Acta Crystallogr. D Biol. Crystallogr. 59, 1124–1130.

Pettersen, E.F., Goddard, T.D., Huang, C.C., Couch, G.S., Greenblatt, D.M., Meng, E.C., and Ferrin, T.E. (2004). UCSF Chimera—a visualization system for exploratory research and analysis. J. Comput. Chem. 25, 1605–1612.

Pintilie, G., and Chiu, W. (2012). Comparison of Segger and other methods for segmentation and rigid-body docking of molecular components in cryo-EM density maps. Biopolymers 97, 742–760.

Pintilie, G., Chen, D.H., Haase-Pettingell, C.A., King, J.A., and Chiu, W. (2016). Resolution and Probabilistic Models of Components in CryoEM Maps of Mature P22 Bacteriophage. Biophys. 110, 827–839.

Preston, G.M., Guerriero, C.J., Metzger, M.B., Michaelis, S., and Brodsky, J.L. (2018). Substrate insolubility dictates Hsp104-dependent endoplasmic-reticulum-associated degradation. Mol. Cell 70, 242–253.e6.

Ruan, L., Zhou, C., Jin, E., Kucharavy, A., Zhang, Y., Wen, Z., Florens, L., and Li, R. (2017). Cytosolic proteostasis through importing of misfolded proteins into mitochondria. Nature 543, 443–446.

Scheres, S.H. (2012). RELION: implementation of a Bayesian approach to cryo-EM structure determination. J. Struct. Biol. 180, 519–530.

Schirmer, E.C., Homann, O.R., Kowal, A.S., and Lindquist, S. (2004). Dominant gain-of-function mutations in Hsp104p reveal crucial roles for the middle region. Mol. Biol. Cell 15, 2061–2072.

Schirmer, E.C., Lindquist, S., and Vierling, E. (1994). An Arabidopsis heat shock protein complements a thermotolerance defect in yeast. Plant Cell 6, 1899–1909.

Shorter, J., and Lindquist, S. (2004). Hsp104 catalyzes formation and elimination of self-replicating Sup35 prion conformers. Science 304, 1793–1797.

Sondheimer, N., and Lindquist, S. (2000). Rnq1: an epigenetic modifier of protein function in yeast. Mol. Cell 5, 163–172.

Sweeny, E.A., Jackrel, M.E., Go, M.S., Sochor, M.A., Razzo, B.M., DeSantis, M.E., Gupta, K., and Shorter, J. (2015). The Hsp104 N-terminal domain enables disaggregase plasticity and potentiation. Mol. Cell 57, 836–849.

Sweeny, E.A., and Shorter, J. (2016). Mechanistic and structural insights into the prion-disaggregase activity of Hsp104. J. Mol. Biol. 428, 1870–1885.

Tang, G., Peng, L., Baldwin, P.R., Mann, D.S., Jiang, W., Rees, I., and Ludtke, S.J. (2007). EMAN2: an extensible image processing suite for electron microscopy. J. Struct. Biol. 157, 38–46.

Tariq, A., Lin, J., Noll, M.M., Torrente, M.P., Mack, K.L., Murillo, O.H., Jackrel, M.E., and Shorter, J. (2018). Potentiating Hsp104 activity via phosphomimetic mutations in the middle domain. FEMS Yeast Res. 18, https://doi.org/10.1093/femsyr/foy042.

Terwilliger, T.C., Grosse-Kunstleve, R.W., Afonine, P.V., Moriarty, N.W., Adams, P.D., Read, R.J., Zwart, P.H., and Hung, L.W. (2008). Iterative-build OMIT maps: map improvement by iterative model building and refinement without model bias. Acta Crystallogr. D Biol. Crystallogr. 64, 515–524.

Terwilliger, T.C., Read, R.J., Adams, P.D., Brunger, A.T., Afonine, P.V., Grosse-Kunstleve, R.W., and Hung, L.W. (2012). Improved crystallographic models through iterated local density-guided model deformation and reciprocal-space refinement. Acta Crystallogr. D Biol. Crystallogr. 68, 861–870.

Torrente, M.P., Chuang, E., Noll, M.M., Jackrel, M.E., Go, M.S., and Shorter, J. (2016). Mechanistic insights into Hsp104 potentiation. J. Biol. Chem. 291, 5101–5115.

Trabuco, L.G., Villa, E., Mitra, K., Frank, J., and Schulten, K. (2008). Flexible fitting of atomic structures into electron microscopy maps using molecular dynamics. Structure 16, 673–683.

Trabuco, L.G., Villa, E., Schreiner, E., Harrison, C.B., and Schulten, K. (2009). Molecular dynamics flexible fitting: a practical guide to combine cryo-electron microscopy and X-ray crystallography. Methods 49, 174–180.

van den Boom, J., and Meyer, H. (2018). VCP/p97-mediated unfolding as a principle in protein homeostasis and signaling. Mol. Cell 69, 182–194.

Wendler, P., Shorter, J., Plisson, C., Cashikar, A.G., Lindquist, S., and Saibil, H.R. (2007). Atypical AAA+ subunit packing creates an expanded cavity for disaggregation by the protein-remodeling factor Hsp104. Cell 131, 1366–1377.

Wendler, P., Shorter, J., Snead, D., Plisson, C., Clare, D.K., Lindquist, S., and Saibil, H.R. (2009). Motor mechanism for protein threading through Hsp104. Mol. Cell 34, 81–92.

Winn, M.D., Ballard, C.C., Cowtan, K.D., Dodson, E.J., Emsley, P., Evans, P.R., Keegan, R.M., Krissinel, E.B., Leslie, A.G., McCoy, A., et al. (2011). Overview of the CCP4 suite and current developments. Acta Crystallogr. D Biol. Crystallogr. 67, 235–242.

Yokom, A.L., Gates, S.N., Jackrel, M.E., Mack, K.L., Su, M., Shorter, J., and Southworth, D.R. (2016). Spiral architecture of the Hsp104 disaggregase reveals the basis for polypeptide translocation. Nat. Struct. Mol. Biol. 23, 830–837.

Yu, H.Y., Ziegelhoffer, T., Osipiuk, J., Ciesielski, S.J., Baranowski, M., Zhou, M., Joachimiak, A., and Craig, E.A. (2015). Roles of intramolecular and intermolecular interactions in functional regulation of the Hsp70 J-protein co-chaperone Sis1. J. Mol. Biol. 427, 1632–1643.

Zakas, P.M., Brown, H.C., Knight, K., Meeks, S.L., Spencer, H.T., Gaucher, E.A., and Doering, C.B. (2017). Enhancing the pharmaceutical properties of protein drugs by ancestral sequence reconstruction. Nat. Biotechnol. *35*, 35–37.

Zehr, E., Szyk, A., Piszczek, G., Szczesna, E., Zuo, X., and Roll-Mecak, A. (2017). Katanin spiral and ring structures shed light on power stroke for microtubule severing. Nat. Struct. Mol. Biol. *24*, 717–725.

Zhang, K. (2016). Gctf: real-time CTF determination and correction. J. Struct. Biol. *193*, 1–12.

Zhao, X., Rodriguez, R., Silberman, R.E., Ahearn, J.M., Saidha, S., Cummins, K.C., Eisenberg, E., and Greene, L.E. (2017). Heat shock protein 104 (Hsp104)-mediated curing of [PSI(+)] yeast prions depends on both [PSI(+)] conformation and the properties of the Hsp104 homologs. J. Biol. Chem. *292*, 8630–8641.

Zheng, S.Q., Palovcak, E., Armache, J.P., Verba, K.A., Cheng, Y., and Agard, D.A. (2017). MotionCor2: anisotropic correction of beam-induced motion for improved cryo-electron microscopy. Nat. Methods *14*, 331–332.

STAR★METHODS

KEY RESOURCES TABLE

REAGENT or RESOURCE	SOURCE	IDENTIFIER
Antibodies		
Mouse monoclonal anti-FLAG M2	Sigma-Aldrich	Cat# F1804; RRID: AB_262044
Rabbit polyclonal anti-TDP-43	Proteintech	Cat# 10782-2-AP; RRID: AB_615042
Rabbit polyclonal anti-GFP	Sigma-Aldrich	Cat# G1544; RRID: AB_439690
Mouse monoclonal 3-phosphoglycerate kinase	Novex	Cat# 459250; RRID: AB_221541
Rabbit polyclonal anti-Rnq1	(Sondheimer and Lindquist, 2000)	N/A
Fluorescently labeled anti-mouse secondary antibodies	Li-Cor	Cat# 926-32210; RRID: AB_621842
Fluorescently labeled anti-rabbit secondary antibodies	Li-Cor	Cat# 926-68071; RRID: AB_10956166
Deposited Data		
The Crystal Structure of ClpB N Terminal Domain	PDB, to be published	PDB: 1KHY
Crystal Structure Analysis of ClpB	(Lee et al., 2003)	PDB: 1QVR
Negative-stain electron microscopy of *E. coli* ClpB mutant E432A	(Carroni et al., 2014)	PDB: 4D2Q
Negative-stain electron microscopy of *E. coli* ClpB	(Carroni et al., 2014)	PDB: 4D2U
Bacterial and Virus Strains		
E. coli BL21 (DE3) cells	Agilent	Cat# 200131
E. coli BL21 (DE3) RIL cells	Agilent	Cat# 230245
Chemicals, Peptides, and Recombinant Proteins		
Sepharose High Performance Nickel Beads	GE Healthcare	Cat# 17-5268-02
Affi-Gel Blue Media	BioRad	Cat# 153-7301
Lysozyme	Sigma-Aldrich	Cat# L6876
Firefly luciferase	Sigma-Aldrich	Cat# L-9506
Creatine kinase	Roche	Cat# 10127566001
Creatine phosphate	Roche	Cat# 10621722001
cOmplete Mini, EDTA-free protease inhibitor	Roche	Cat# 11835170001
Zymolyase 100 T	MP Biomedicals	Cat# 0832093
Protease inhibitor cocktail for fungal and yeast extracts	Sigma-Aldrich	Cat# P8215
ATP	Sigma-Aldrich	Cat# A3377
His$_6$-(TevC)-*Ct*Hsp104	This paper	N/A
His$_6$-(TevC)-*Ct*Hsp104$^{R328M:R757M}$/His$_6$-(TevC)-*Ct*Hsp104^{2R}	This paper	N/A
His$_6$-(TevC)-*Ct*Hsp104$^{\Delta N}$	This paper	N/A
His$_6$-(TevC)-*Ct*Hsp104$^{\Delta N:\Delta C}$	This paper	N/A
His$_6$-(TevC)-*Ct*Hsp104$^{\Delta N:DWB}$	This paper	N/A
His$_6$-(TevC)-*Ct*Hsp104$^{\Delta N:2R}$	This paper	N/A
*Sc*Hsp104	(Jackrel et al., 2014)	N/A
His$_6$-SUMO-Ssa1	This paper	N/A
His$_6$-SUMO-Hsc70	This paper	N/A
His$_6$-SUMO-Sis1	This paper	N/A
His$_6$-SUMO-Ydj1	This paper	N/A
His$_6$-SUMO-Hdj1	This paper	N/A

Continued

REAGENT or RESOURCE	SOURCE	IDENTIFIER
His$_6$-SUMO-Hdj2	This paper	N/A
PAP(248-286) to make SEVI fibers	Keck Biotechnology Resource Laboratory, Yale University	N/A
Critical Commercial Assays		
PiColorLock Phosphate Detection	Innova/Expedeon	Cat# 303
Luciferase assay reagent	Promega	Cat# E1483
Deposited Data		
CryoEM structure of *Ct*Hsp104	This paper	EMD-7782/PDB: 6D00
X-ray crystal structure of *Ct*Hsp104^{2R} complex with ADP	This paper	PDB: 6AZY
Experimental Models: Organisms/Strains		
W303a (*MATa, can1-100, his3-11, 15, leu2-3, 112, trp1-1, ura3-1, ade2-1*)	(Schirmer et al., 2004)	N/A
W303aΔ*hsp104* (*MATa can1-100, his3-11, 15, leu2-3, 112, trp1-1, ura3-1, ade2-1, hsp104::KanMX*)	(Schirmer et al., 2004)	A3224
Oligonucleotides		
*Ct*Hsp104, 153-882 construct was created using forward primer - TACTTCCAATCCAATGCCGCAGAGGAGGCGTACGAGG and reverse primer - TTATCCACTTCCAATGTTAGATTTCCATATCCTCGTCTTCAACCATG	This paper	N/A
*Ct*Hsp104, 153-864 construct was created using forward primer - TACTTCCAATCCAATGCCGCAGAGGAGGCGTACGAGG and reverse primer - TTATCCACTTCCAATGTTATTCGATCCCGTGGTTGCGGAT	This paper	N/A
Recombinant DNA		
pMCSG68	(Kim et al., 2011)	N/A
*Ct*Hsp104 in pMCSG68	This paper	N/A
*Ct*Hsp104$^{R328M:R757M}$ in pMCSG68	This paper	N/A
*Ct*Hsp104^{ΔN} in pMCSG68	This paper	N/A
*Ct*Hsp104$^{ΔN:ΔC}$ in pMCSG68	This paper	N/A
*Ct*Hsp104$^{ΔN:DWB}$ in pMCSG68	This paper	N/A
*Ct*Hsp104$^{ΔN:2R}$ in pMCSG68	This paper	N/A
*Sc*Hsp104 in pNOTAG	(Jackrel et al., 2014)	N/A
pE-SUMO	LifeSensors	N/A
Ssa1 in pE-SUMO	This paper	N/A
Hsc70 in pE-SUMO	This paper	N/A
Sis1 in pE-SUMO	This paper	N/A
Ydj1 in pE-SUMO	This paper	N/A
Hdj1 in pE-SUMO	This paper	N/A
Hdj2 in pE-SUMO	This paper	N/A
pAG416GAL-Hsp104-FLAG	This paper	N/A
pAG416GAL-Hsp104^{A503V}-FLAG	This paper	N/A
pAG416GAL-Hsp104^{A503S}-FLAG	This paper	N/A
pAG416GAL-*Ct*Hsp104-FLAG	This paper	N/A
pAG303GAL-TDP43	(Johnson et al., 2009)	N/A
pAG303GAL-α-Syn-YFP	(Gitler et al., 2008)	N/A

REAGENT or RESOURCE	SOURCE	IDENTIFIER
pAG304GAL-α-Syn-YFP	(Gitler et al., 2008)	N/A
pAG416GAL-103Q-CFP	(Duennwald et al., 2006)	N/A
Software and Algorithms		
HKL3000 suite	(Minor et al., 2006)	N/A
Ctruncate program	(French and Wilson, 1978; Padilla and Yeates, 2003)	N/A
CCP4 package	(Winn et al., 2011)	N/A
Phaser	(McCoy et al., 2007)	N/A
Buccaneer	(Cowtan, 2006)	N/A
Coot	(Emsley and Cowtan, 2004)	N/A
Phenix	(Afonine et al., 2012)	N/A
EMAN2	(Tang et al., 2007)	http://blake.bcm.edu/emanwiki/EMAN2/
Relion	(Scheres, 2012)	https://www2.mrc-lmb.cam.ac.uk/relion/index.php/Main_Page
Chimera	(Pettersen et al., 2004)	https://www.cgl.ucsf.edu/chimera/
Segger	(Pintilie and Chiu, 2012)	https://cryoem.slac.stanford.edu/ncmi/resources/software/segger
Molecular Dynamics flexible Fitting	(Trabuco et al., 2009)	https://www.ks.uiuc.edu/Research/mdff/
ProMod	(Pintilie and Chiu, 2012)	https://cryoem.slac.stanford.edu/ncmi/resources/software/segger
Other		
Superdex-200 10/300GL	GE Healthcare	Cat# 17-9909-44
Hiload 16/60 Superdex 200	GE Healthcare	Cat# 17-1069-01
Sepharose High Performance Nickel Beads	GE Healthcare	Cat# 17-5268-02
Affi-Gel Blue Media	BioRad	Cat# 153-7301
MCSG crystallization screens	Anatrace	MCSG-1 MCSG-2 MCSG-3 MCSG-4

CONTACT FOR REAGENT AND RESOURCE SHARING

Requests for resources, reagents, and further information should be directed to, and will be fulfilled by Andrzej Joachimiak (andrzejj@anl.gov) or James Shorter (jshorter@pennmedicine.upenn.edu).

EXPERIMENTAL MODEL AND SUBJECT DETAIL

Yeast Strains and Media
All yeast strains were WT W303a (*MATa*, *can1-100*, *his3-11*, *15*, *leu2-3*, *112*, *trp1-1*, *ura3-1*, *ade2-1*) or the isogenic strain W303a*Δhsp104* (Schirmer et al., 2004). Yeast were grown in rich media (YPD) or in synthetic media lacking L-histidine and uracil, and containing 2% glucose (SD-His-Ura), raffinose (SRaf-His-Ura) or galactose (SGal-His-Ura).

METHOD DETAILS

Plasmids
The gene encoding *Ct*Hsp104 was amplified from *C. thermophila* cDNA (a gift from Dr. Adrian Tsang, Concordia University) via PCR and inserted into pMCSG68 vector (Kim et al., 2011). The R328M/R757M double mutant (*Ct*Hsp104[2R]) was created using modified PIPE cloning previously described (Klock and Lesley, 2009). The presence of both mutations was confirmed by sequencing at University of Chicago Cancer Research DNA Sequencing Facility. The expression vectors were transformed into *E. coli* BL21-Gold (DE3) cells (Agilent). The N- and C-terminal truncations were produced from the full-length gene using the following set of primers: the 153-882 construct was created using forward (TACTTCCAATCCAATGCCGCAGAGGAGGCGTACGAGG) and reverse (TTATCCACTTCCAATGTTAGATTTCCATATCCTCGTCTTCAACCATG) primers and the 153-864 construct was created using

forward (TACTTCCAATCCAATGCCGCAGAGGAGGCGTACGAGG) and reverse (TTATCCACTTCCAATGTTATTCGATCCCG TGGTTGCGGAT) primers and were cloned to vector pMCSG68. Vectors encoding TDP-43, α-Syn, and an expanded polyGlu tract (pAG303GAL-TDP43, pAG303GAL-α-Syn-YFP, pAG304GAL-α-Syn-YFP, and pAG303GAL-103Q-CFP) were from Drs. A. Gitler and M. Duennwald (Duennwald and Lindquist, 2008; Gitler et al., 2008), pAG416GAL-Hsp104, pAG416GAL-Hsp104^{A503V}, and pAG416GAL-Hsp104^{A503S} have been described previously (Jackrel et al., 2014). pAG416G AL-CtHsp104 was generated by Gateway cloning. For this paper, Hsp104 vectors were modified by the addition of a C-terminal 1xFLAG tag to facilitate immunodetection of CtHsp104. Hsp104-FLAG constructs behaved as untagged protein in all assays.

CtHsp104^{2R} Preparation for Crystallization

30 mL of LB-phosphate media containing 10 g tryptone, 5 g yeast extract, 5 g NaCl (BioShop), 40 mM K$_2$HPO$_4$ (BioShop), 0.5% glucose (Sigma Aldrich), 150 mg ampicillin (BioShop) per liter was inoculated with 100 μL of overnight starter E. coli culture expressing CtHsp104^{2R} and was grown at 37°C, 200 rpm. After 16 h, large scale cultures were inoculated by adding 30 mL small scale overnight culture to 1 L LB-phosphate media. Cultures were grown at 37°C, 190 rpm to OD$_{600}$ 1.0, and cooled to 18°C prior to overnight induction with 0.5 mM isopropyl 1-thio-β-D-galactopyranoside (IPTG) at 18°C, 180 rpm. Cells were harvested via centrifugation at 6,500 rpm, 4°C for 10 minutes and resuspended in 30 mL lysis buffer (50 mM HEPES-NaOH pH 8.0, 500 mM NaCl, 5% (v/v) glycerol, 20 mM imidazole, and 10 mM β-mercaptoethanol (β-ME), plus 1 protease inhibitor cocktail tablet (cOmplete ULTRA, Roche, Indianapolis, Indiana, USA)). Resuspended cells were stored at –80°C prior to protein purification.

Frozen cells were thawed, supplemented with lysozyme (final concentration 1 mg/mL) and lysed on ice for 1 h. Lysate was sonicated on ice with 4 s bursts, followed by a 20 s pause, for 4 min. Cells were then centrifuged at 13,000 rpm for 90 min followed by filtration through 0.45 μm syringe filters. Clarified lysate was manually purified using the vacuum assisted purification system and Sepharose High Performance Nickel Beads (GE Healthcare Life Sciences, Piscataway, NJ, USA) on ice. Column was washed with water, and pre-equilibrated with lysis buffer (50 mM HEPES-NaOH pH 8.0, 500 mM NaCl, 5% (v/v) glycerol, 20 mM imidazole, and 10 mM β-ME) and protein was eluted with buffer containing 250 mM imidazole pH 8.0. Fractions containing CtHsp104^{2R} were pooled and digested with recombinant His$_7$-tagged TEV protease, at the ratio 1 mg/25 mg of target protein. The completeness of the His$_6$-tag digestion was verified by SDS-PAGE and CtHsp104^{2R} was dialyzed overnight against desalting buffer (50 mM HEPES-NaOH pH 8.0, 500 mM NaCl, 5% (v/v) glycerol, and 10 mM β-ME) at 4°C to remove the His$_6$-tag. The resulting protein carries the N-terminal SNA sequence artifact. The CtHsp104^{2R} protein was concentrated to 1.5 mL on Amicon Ultra-15 centrifugal concentrators (Millipore, Bedford, MA, USA) and further purified using size exclusion chromatography (SEC) on Superdex 200 column (GE Healthcare Life Sciences, Piscataway, NJ, USA) pre-equilibrated with desalting buffer to remove the His$_7$-tagged TEV protease and other small molecular weight contaminants. The CtHsp104^{2R} fractions containing monomeric protein were then concentrated using Amicon Ultra-15 concentrators (Millipore, Bedford, MA, USA) and buffer-exchanged with a crystallization buffer containing 20 mM HEPES-NaOH pH 8.0, 200 mM KCl, 4 mM dithiothreitol (DTT). Glycerol was then added to a final concentration of 10% prior to cryo-cooling the protein in liquid nitrogen and storage at -80°C.

Preparation of CtHsp104 and Deletion Mutants for Cryo-EM, SEC and DLS

The 30 mL of LB-phosphate media culture of CtHsp104 and deletion mutants were prepared as described above. After 16 h, large scale cultures were prepared by adding 30 mL small scale over-night culture to 1 L LB-phosphate media, prepared as above. Cell cultures were grown at 37°C, 200 rpm to OD$_{600}$ 1.0, and cooled to 15°C prior to their induction with 0.5 mM IPTG. Cultures were allowed to grow at 15°C, 180 rpm overnight. Cells were harvested via centrifugation at 4,500 rpm, 4°C for 20 min and resuspended in 35 mL lysis buffer containing 20 mM HEPES-KOH pH 7.57, 20 mM KCl (mutants) or 100 mM KCl (WT), 5% (v/v) glycerol, 20 mM imidazole pH 8.0, 2 mM MgCl$_2$, 0.5 mM ATP pH 8.0 and 10 mM β-ME. Resuspended cells were stored at –80°C prior to their purification. Frozen cells were thawed and sonicated on ice with 2 s bursts, followed by a 20 s pause, for 3 min. Cells were then centrifuged at 13,000 rpm for 90 min followed by filtration through 0.45 μm syringe filters. Clarified lysate was manually purified as described above. The nickel column was pre-equilibrated with lysis buffer and eluted with elution buffer containing 250 mM imidazole pH 8.0. Collected fractions were digested with recombinant His-tagged TEV protease, 1 mg for every 25 mg of target protein overnight. Sample was concentrated down to 1.5 mL using Amicon Ultra-15 100K concentrators (Millipore, Bedford, MA, USA) and further purified via size exclusion chromatography (see below). The fractions containing CtHsp104 hexamer (∼664kDa WT) were then collected and concentrated using 100K concentrators and buffer-exchanged with a buffer containing 20 mM HEPES-KOH 7.57, 20 mM KCl (mutants) or 100 mM KCl (WT), 2 mM MgCl$_2$, 2 mM ATP pH 8.0 and 4 mM DTT.

The samples were further characterized biophysically to determine conditions that support oligomerization. Due to the addition of nucleotide, the final CtHsp104 concentration (60.9 mg/mL) was determined via the colorimetric, bicinchoninic acid (BCA) protein assay @562nm (Pierce, ThermoFisher Scientific). Dynamic light scattering (DLS) (DynaPro Plate Reader, Wyatt) was used to identify dilutions suitable for cryo-EM single particle imaging. The DLS experiments were performed at 23°C. CtHsp104, CtHsp104^{ΔN}, CtHsp104$^{ΔN:ΔC}$, CtHsp104$^{ΔN:DWB}$ and CtHsp104$^{ΔN:2R}$ (Table S1) were diluted using 20 mM HEPES-KOH pH 7.57, 20 mM KCl (mutants) or 100 mM KCl (WT), 2 mM ATP pH 8.0, 2 mM MgCl$_2$, and 4 mM DTT to 0.5 mg/mL, 1 mg/mL and 5 mg/mL.

Size Exclusion Chromatography of CtHsp104 and Deletion Mutants

Size-exclusion chromatography (SEC) was performed on a Superdex-200 10/300GL column using AKTAxpress (GE Healthcare). The column was pre-equilibrated with buffer containing 20 mM HEPES-KOH pH 7.5, 20 mM KCl (mutants) or 100 mM KCl (WT),

5% glycerol, 20 mM imidazole, pH 8.0, 0.5 mM ATP pH 8.0, 2 mM MgCl$_2$, and 10 mM β-ME. The column was calibrated with premixed protein standards, including catalase (230 kDa), ferritin (440 kDa), and thyroglobulin (660 kDa). A 1.5 mL protein sample was injected into the column. The chromatography was carried out at room temperature at a flow rate of 1.5 mL/min. The calibration curve of Kav versus log molecular weight was prepared using the equation Kav=(Ve−Vo)/(Vt−Vo), where Ve is the elution volume for the protein, Vo is the column void volume, and Vt is the total bed volume. The *Ct*Hsp104, *Ct*Hsp104^{ΔN}, *Ct*Hsp104$^{ΔN:ΔC}$, *Ct*Hsp104$^{ΔN:DWB}$ and *Ct*Hsp104$^{ΔN:2R}$ migrate the SEC column as hexamers (Table S1).

Protein Crystallization

*Ct*Hsp104^{2R} variant was screened for crystallization using a Mosquito nanoliter liquid handler (TTP Labtech, Cambridge, MA) using the sitting drop vapor diffusion technique in 96-well CrystalQuick plates (Greiner Bio-one, Monroe, NC). Prior to setting up crystallization, *Ct*Hsp104^{2R} was diluted to 15 mg/mL and incubated with 5 mM ADP and 10 mM MgCl$_2$ for 10 min at 40°C. For each condition, 0.5 μL of protein and 0.5 μL of crystallization formulation were mixed; the mixture was equilibrated against 135 μL of the crystallization solution in each reservoir well. The crystallization screens MCSG-1-4 ((Anatrace, Maumee, OH)) were used for screening at 4°C and 16°C. Crystals appeared under MCSG-2 condition containing 0.2 M calcium acetate, 0.1 M MES-NaOH pH 6.0, and 10% propanol at 4°C.

X-ray Data Collection, Structure Determination and Refinement

Prior to flash-cooling in liquid nitrogen, *Ct*Hsp104^{2R} crystals were cryo-protected in mother liquor supplemented with 35% glycerol. The X-ray diffraction data collection was carried out at the Structural Biology Center 19-ID beamline at the Advanced Photon Source, Argonne National Laboratory. The data were collected at 100K at 0.9726 Å wavelength. The diffraction images were processed with the HKL3000 suite (Minor et al., 2006). Intensities were converted to structure factor amplitudes in the Ctruncate program (French and Wilson, 1978; Padilla and Yeates, 2003) from the CCP4 package (Winn et al., 2011).

The structure was solved by molecular replacement using Phaser (McCoy et al., 2007) with *Tt*ClpB (PDB: 1QVR, (Lee et al., 2003)) and *E. coli* (PDB: 1KHY) as search models. Specifically, the 1QVR template was divided into 6 domains. First, NBD1 (residues 153-330) and NBD2 (residues 331-396, 511-540) were identified. This solution was used as a starting point to search for CTT (residues 756-850) and subsequently to search MD (residues 397-510) and NTD (with 1KHY as a model). The resulting solution was morphed into the electron density map (Terwilliger et al., 2012) and rebuilt in Buccaneer (Cowtan, 2006). An additional round of Phaser with Buccaneer-derived structure used as a fixed partial solution enabled the localization of additional residues (residues 543-578, 588-636, 651-686, 700-709, 740-755). In the next step, morphing and autobuilding was used (Adams et al., 2013; Terwilliger et al., 2008). Finally, iterative manual structure corrections in Coot (Emsley and Cowtan, 2004) and crystallographic refinement in Phenix (Afonine et al., 2012) was applied to improve the model. The refinement protocol included optimization of TLS parameters, with the protein chain divided into 5 groups. In the final model, 810/882 (92%) of residues were included, corresponding to the following fragments: Ser2-Asp75, Glu80-Gly144, Ala156-Ala247, Gly251-Ala282, Ala288-Leu647, Gly661-Leu721, Thr738-Ile863 (Figure 1). In ordered segments, the majority of amino-acid side chains are well defined in the electron density. The missing segments are disordered in the crystal lattice. The data collection, processing and refinement statistics are given in Table 2.

Cryo-Electron Microscopy Data Acquisition

The samples were initially screened at the Advanced Electron Microscopy facility at the University of Chicago, National Center for Protein Science Shanghai and data collection was performed at the National Center for Macromolecular Imaging at SLAC-Stanford. Two microliter samples of *Ct*Hsp104 hexamer (0.5 mg/mL) in a buffer 100 mM KCl, 2 mM MgCl$_2$, 2 mM ATP pH 8.0 and 4 mM DTT were applied onto glow-discharged 200-mesh R2/1 Quantifoil grids. The grids were blotted for 3 s and rapidly cryo-cooled in liquid ethane using a Vitrobot Mark IV (Neumann et al., 2006). The samples were screened using Talos Arctica cryo-electron microscope (Neumann et al., 2006) operated at 200 kV and then imaged in a Titan Krios cryo-electron microscope (Neumann et al., 2006) with GIF energy filter (Gatan) at a magnification of 130,000× (corresponding to a calibrated sampling of 1.06 Å per pixel). Micrographs were recorded with a Gatan K2 Summit direct electron detector, where each image is composed of 30 individual frames with an exposure time of 6 s and a dose rate of 5.3 electrons per second per Å^2. A total of 3,186 video stacks were collected with a defocus range of 0.8-2.8 μm.

Single Particle Image Processing and 3D Reconstruction

All micrographs were motion-corrected using MotionCor2 (Zheng et al., 2017) and CTF-corrected using Gctf (Zhang, 2016). Initial particles data set was picked manually using EMAN2 (Tang et al., 2007), which yielded ~3,000 particles from 50 micrographs. 25 2D-class averages, determined by RELION (Scheres, 2012), were used to generate an initial model in EMAN2. Then, the initial model was used for template-automated particle picking in EMAN2, yielding a ~377,000-particle data set from the selected 2,716 micrographs. Then, particle coordinates were imported to RELION, where the 2D/3D classification and 3D refinement were performed. After removing poor 2D class averages by 2D classification for 3 times, a total data set of ~260,000 particles was used for 3D refinement, generating the 4.1 Å map. Further 3D classification with C1 symmetry using the 4.1 Å map with 60 Å low-pass filter as an initial model was used to remove a bad class with 13.5% of the particle set. Next, final 3D refinement was performed using 224,915 particles, 4.4 Å map without mask and 4.0 Å map with mask were achieved.

Segmentation and Fitting

The reconstructed 3D density map was segmented using Segger (Pintilie and Chiu, 2012) and UCSF Chimera (Pettersen et al., 2004) generating a rough initial estimate of the 6 protomers expected in the assembly. Six copies of the crystallographic monomer structure were then rigidly fitted to the map by alignment to each of the 6 segmented regions. Secondary structure elements matched well between the fitted models and the map, especially in the NBDs. The NTD in the crystal model were well outside the cryo-EM density, since it has a drastically different position in the crystallographic structure. The NTD in the cryo-EM density is at a lower resolution, and secondary structures are not clearly visible as in the NBDs. Local exhaustive search (using the Fit to Segments tool in Segger) was thus used to determine the position and orientation of each of the 6 protomers in the density; moderate Z-scores (2-3) indicated reasonable confidence in the final placements. These placements also agreed with previous cryo-EM maps (Yokom et al., 2016). The 6 independently fitted protomers were then joined into one model (chains P1 - P6), also taking the ADP ligands from the crystal model (chains A-F).

Each of the 6 rigidly fitted protomers however, appeared to have a slightly different conformation in the cryo-EM density. Hence we then applied the Molecular Dynamics Flexible Fitting, or MDFF (Trabuco et al., 2008). We applied the method in 10 independent runs, to be able to calculate the uncertainty in the resulting model (Video S2). Each run consisted of 10^4 minimization steps followed by 10^5 molecular dynamics steps, after which the model stopped deforming significantly. The resulting 10 structures were then input into ProMod (Pintilie et al., 2016) to produce a probabilistic model, which measures the uncertainty at each atom position given the 10 possible results.

Proteins for Biochemical Assays

Untagged Hsp104 from *S. cerevisiae* was expressed and purified as described previously (DeSantis et al., 2014; Jackrel et al., 2014; Torrente et al., 2016). *Ct*Hsp104 was purified from BL21(DE3)RIL cells grown in 2xYT broth supplemented with 25 μg/mL chloramphenicol and 100 μg/mL ampicillin. Protein expression was induced at an OD_{600} of 0.4-0.6 with 1 mM IPTG for 16 h at 15°C. Cells were harvested by centrifugation (4,000 g, 4°C, 20 min), resuspended in lysis buffer (40 mM HEPES-KOH pH 7.4, 500 mM KCl, 20 mM $MgCl_2$, 2.5% glycerol, 20 mM imidazole, 2 mM β-ME) supplemented with 5 μM pepstatin A and complete protease inhibitor tablets (Gitler et al.). All purification steps were carried out at 4°C. Cells were lysed by incubation with 1 mg/mL hen egg lysozyme and sonication. Lysate was clarified by centrifugation at 16,000 rpm for 20 min and loaded onto Ni-NTA resin. The resin was washed with 10 volumes of wash buffer (40 mM HEPES-KOH pH 7.4, 500 mM KCl, 20 mM $MgCl_2$, 2.5% glycerol, 20 mM imidazole, 2 mM β-ME). Protein was eluted in wash buffer supplemented with 350 mM imidazole. TEV protease was added to eluted protein, and the sample was dialyzed against wash buffer containing no imidazole for 4 h at room temperature followed by ~16 h at 4°C. After dialysis and cleavage, the protein was loaded onto a second Ni-NTA column to remove the His_6 tag and uncleaved protein. Eluted *Ct*Hsp104 was pooled, concentrated, and exchanged into high salt storage buffer (40 mM HEPES-KOH pH 7.4, 500 mM KCl, 20 mM $MgCl_2$, 10% glycerol, and 1 mM DTT). A portion was used immediately for biochemical assays, and the remainder was flash cooled in liquid nitrogen and stored at -80°C until further use.

Ssa1, Hsc70, Sis1, Ydj1, Hdj1, and Hdj2 (in pE-SUMO (Life Sensors)) were expressed as N-terminally His_6-SUMO-tagged proteins in BL21(DE3)RIL cells. Transformed cells were grown at 37°C in LB media supplemented with 25 μg/mL chloramphenicol and 100 μg/mL ampicillin to an OD_{600} ~0.5. Cultures were cooled to 15°C, and expression was induced with 1 mM IPTG for 16 h. Cells were harvested, resuspended in lysis buffer (50 mM HEPES pH 7.5, 750 mM KCl, 5 mM $MgCl_2$, 10% glycerol, 20 mM imidazole, 2 mM β-ME, 5 μM pepstatin A, and complete protease inhibitor (Roche)), and lysed by incubation with hen egg lysozyme followed by sonication. Lysates were clarified by centrifugation (16,000×g, 20 min, 4°C), and incubated with Ni-NTA resin for 90 min at 4°C. Resin was washed with 10 column volumes of wash buffer (50 mM HEPES pH 7.5, 750 mM KCl, 10 mM $MgCl_2$, 10% glycerol, 20 mM imidazole, 1 mM ATP, 2 mM β-ME) and eluted with 2 column volumes of elution buffer (wash buffer+300 mM imidazole). To cleave the His_6-SUMO tag, Ulp1 was added at a 1:100 molar ratio, and imidazole was removed by dialysis against wash buffer. After dialysis, protein was loaded onto a 5 mL HisTrap column (GE Healthcare) and eluted with a linear imidazole gradient (20-350 mM) over 40 column volumes. Fractions containing cleaved protein were pooled, concentrated, and purified further by Resource Q (Ssa1, Hsc70, Ydj1, and Hdj2) or Resource S (Sis1 and Hdj1) ion exchange chromatography.

ATPase Assay

*Ct*Hsp104 (0.042 mM hexamer) was incubated with ATP (1 mM) for 5 min at the indicated temperatures in luciferase-refolding buffer (LRB): 25 mM HEPES-KOH pH 7.4, 150 mM potassium acetate, 10 mM magnesium acetate, 10 mM DTT. ATPase activity was assessed by the release of inorganic phosphate, which was determined using a malachite green phosphate detection kit (Innova). Background hydrolysis was determined at time zero and subtracted.

Luciferase Reactivation Assay

Luciferase reactivation was performed as described (DeSantis et al., 2012). To assemble aggregates, firefly luciferase (Sigma; 100 μM) in LRB (25 mM HEPES-KOH pH 7.4, 150 mM potassium acetate, 10 mM magnesium acetate, 10 mM DTT) plus 6 M urea was incubated at 30°C for 30 min. The sample was then rapidly diluted 100-fold into LRB. Aliquots were snap-cryo-cooled and stored at -80°C until use. Aggregated luciferase (100 nM) was incubated with *Ct*Hsp104 (0.167 μM hexamer) with ATP (5.1 mM) and an ATP regeneration system (1 mM creatine phosphate, 0.25 μM creatine kinase (Roche)) in the presence or absence of Hsp70 (either Ssa1 or Hsc70, 0.167 μM), and Hsp40 (either 0.073 μM each Hdj1 and Hdj2 or 0.073 μM each Sis1 and Ydj1) for

90 min at 25°C. After 90 min, luciferase activity was assessed with a luciferase assay system (Promega). Recovered luminescence was monitored using a Tecan Safire plate reader. In some reactions, Hsp70 and Hsp40 were not present, and *Ct*Hsp104 concentration was increased to 1 μM hexamer, and ATP was replaced by a 1:1 mixture of ATP and ATPγS (to a total nucleotide concentration of 5 mM).

Semen-Derived Enhancer of Virus Infection (SEVI) Remodeling

SEVI remodeling was performed as previously described (Castellano et al., 2015). SEVI fibrils (20 μM monomer) were incubated with *Sc*Hsp104 or *Ct*Hsp104 (3 μM hexamer) in LRB buffer in the presence of ATP (5 mM) and an ATP regeneration system (0.1 mM ATP, 0.02 mg/mL creatine kinase, 10 mM creatine phosphate). Samples were incubated at 37°C for the duration of the experiments. At various time points, aliquots were removed, added to a 96-well plate containing a solution of 25 μM ThT in LRB buffer. ThT fluorescence characteristics were measured on a Tecan Safire^2 microplate reader with excitation and emission filters set to 440 nm and 482 nm, respectively. To assess fibril morphology by negative stain EM, reaction aliquots were spotted on Formvar carbon-coated grids (EM Sciences) and stained with 2% uranyl acetate. Samples were visualized using a JEOL-1010 electron microscope.

Yeast Strains and Media

All yeast strains were WT W303a (*MATa, can1-100, his3-11, 15, leu2-3, 112, trp1-1, ura3-1, ade2-1*) or the isogenic strain W303aΔ*hsp104*. Yeast were grown in rich media (YPD) or in synthetic media lacking the appropriate amino acids. Media was supplemented with 2% glucose, raffinose or galactose.

Yeast Transformation and Spotting Assays

Yeast were transformed according to standard protocols using polyethylene glycol and lithium acetate (Gietz and Schiestl, 2007). For spotting assays, yeast were grown to saturation overnight in synthetic raffinose dropout media at 30°C. Cultures were serially diluted 5-fold and spotted in duplicate onto synthetic dropout media containing glucose or galactose. Plates were analyzed after growth for 2-3 days at 30°C.

Thermotolerance

Thermotolerance assays were performed essentially as described (Schirmer et al., 1994), with some modifications. W303aΔ*hsp104* yeast were transformed with plasmids bearing either Hsp104 from *S. cerevisiae* or *C. thermophila* under the native *HSP104* promoter (e.g. pRS313HSE-*Sc*Hsp104-FLAG or pRS313HSE-*Ct*Hsp104-FLAG), or an empty vector control. Transformants were selected, grown to saturation in yeast minimal media SD-His, and then diluted to OD_{600}=0.2 in SD-His. Yeast were allowed to double at 30°C (~4 h), after which cultures were normalized. Cells were then heat shocked at 50°C for 0-60 min and cooled for 2 min on ice. Cultures were diluted 1000-fold, plated on SD-His, and plates were incubated at 30°C for 2-3 days to observe viable colonies.

Semi-Denaturing Detergent Agarose Gel Electrophoresis (SDD-AGE)

SDD-AGE was performed as described (Halfmann and Lindquist, 2008). To prepare lysates, yeast strains were grown to saturation in raffinose dropout media (SRaff-His-Ura) at 30°C, then transferred to 10 mL galactose media (SGal-His-Ura) and grown for an additional 16h to induce polyGlu and Hsp104 expression. Following overnight induction, cells were normalized, washed with sterile water, and resuspended in spheroplasting solution (1.2 M D-sorbitol, 0.5 mM $MgCl_2$, 20 mM Tris pH 7.5, 50 mM β-ME, and 0.5 mg/mL Zymolyase 100T) and incubated for 1 hour at 30°C with intermittent shaking. Spheroplasts were pelleted by centrifugation (500xg for 5 min) and resuspended in lysis buffer (100 mM Tris pH 7.5, 500 mM NaCl, 10 mM β-ME, Protease inhibitor cocktail (Sigma P8215), 10 mM EDTA, 2 mM PMSF, and 0.10% Triton-X 100). This suspension was vortexed at high speed for 2 minutes to lyse spheroplasts. Lysates were combined with 4X sample buffer (2X TAE, 20% glycerol, 8% SDS, 10% β-ME, and 0.0025% bromophenol blue) and incubated for 5 minutes at room temperature. Samples were loaded onto a 1.5% agarose gel in TAE buffer containing 0.1% SDS. The gel was run at 3 V/cm gel length for 5 h. Proteins were transferred to a nitrocellulose membrane by capillary transfer overnight. The nitrocellulose membrane was blocked and probed for Rnq1 conformers with an anti-Rnq1 polyclonal antibody.

QUANTIFICATION AND STATISTICAL ANALYSIS

All data points in each graph are mean ± SEM, and the n is a biological replicate when referring to yeast experiments or an independent experimental trial when referring to biochemical experiments. No statistical significance testing was employed in this study.